



Supplement of

Assessing land elevation in the Ayeyarwady Delta (Myanmar) and its relevance for studying sea level rise and delta flooding

Katharina Seeger et al.

Correspondence to: Katharina Seeger (k.seeger@uni-koeln.de)

The copyright of individual parts of the supplement might differ from the article licence.

S1. Detailed information on material and methods

S1.1. Data

S1.1.1. Elevation data from topographic maps

To investigate land elevation in the Ayeyarwady Delta independently of data derived from global satellite based measurements, we used height information from topographic maps. Beside the series of mappings conducted since the British colonial times that are available to the public, the most recent topographic maps of Myanmar were made and published by the Survey Department, Ministry of Forestry in the Union of Myanmar, in cooperation with the Japan International Cooperation Agency (JICA), and sold by East View Geospatial, Inc. (2014). The maps are at scale of 1:50,000. Map sheets covering the Ayeyarwady Delta were accessed via the Specialised Information Service Cartography and Geodata (SIS Maps) of the Map Department of the *Staatsbibliothek zu Berlin* funded by the German Research Foundation (SIS Maps, 2021). Depending on their location, the data are projected to UTM 46 N or 47 N (based on the WGS84 ellipsoid) while mean sea level (MSL) is used as vertical datum. However, documentation on the date and location of MSL establishment is missing and East View Geospatial, Inc. (2014) only states that source information is “Compiled from best available sources”. Further research on cartographic work and vertical datums in Myanmar turned out Kyaikkhami tide observatory (formerly: Amherst) in eastern Myanmar as reference site (JICA et al., 2004a). As the establishment of the Myanmar 2000 datum involved extensive field surveys, aerial signalisation and photography, levelling, GPS observations and aerial triangulation that were conducted between 2000 and 2004, these data not only constitute source data of topographic maps published by JICA et al. (2004b) but very likely also constitute the source data of topographic maps sold by East View Geospatial, Inc. (2014), which were used in this study. Horizontal accuracy is one-third of contour interval for spot heights and one-half for lines (JICA et al., 2004c). Index contour lines are given in 20 m intervals for elevations higher than 200 m and in 10 m intervals for elevations lower than 200 m (JICA et al., 2004c). Ground control points are accurate at standard deviations of 0.5 m horizontally and 0.3 m vertically (JICA et al., 2004c).

S1.1.2. Global and coastal digital elevation models

In total, 10 DEMs were used to assess their performance in the Ayeyarwady Delta. Table S1 provides an overview of main characteristics such as coverage, resolution, and accuracy as well as information on eventual edits that have been made after DEM generation. Though elevation data from surface and terrain models may show some systematic offset due to the inclusion of canopy and building heights in the digital surface models (DSMs) compared to real ground elevation assessment of digital terrain models (DTMs), we include both types of DEMs into the comparison as these DEMs are the most often used, sometimes without considering that the DEM type should suit the application purpose. Thus, we want to demonstrate the relevance of careful DEM selection as the outcomes of any geomorphological and hydrological study as well as risk assessment and flood

30 modelling will strongly depend on the underlying elevation data (e.g., Wechsler et al., 2007; Siart et al., 2009; Gesch et al., 2018; Brosens et al., 2022).

Table S1. Overview of all elevation models used in this study. DEM = digital elevation model, DSM = digital surface model, DTM = digital terrain model, H = horizontal, V = vertical.

| DEM | Type | Coverage | Acquisition | Technique | Datum | Accuracy | References | Availability |
|------------------|------------|----------------|-----------------------------------------------------------------------------------------------------------------------------------------------------------------------------------------|----------------------------------------------------------------------------------------------------------------------------------------------------------------------------|----------------------|--------------------------------------------------------------------------------------|--------------------------------------------------------------------|----------------|
| SRTM | DSM | 60° N to 56° S | 11/02/2000 to 22/02/2000 | Synthetic Aperture Radar interferometry (dual antennas) | H: WGS84 V: EGM96 | H: 1 arc sec × 1 arc sec (~30 m × 30 m) V: 16 m (LE90), 9.73 m (RMSE) | Farr et al. | Free |
| ACE2 | nearly DTM | 60° N to 60° S | 03/1994 to 08/2002 (Topex Ku band) 04/1994 to 03/1995 (ERS-1) 08/2002 to 07/2005 (Envisat RA- 2 Ku band) 08/2002 to 03/2004 (Jason-1 Ku band) | Correction of SRTM (and GLOBE for regions south of 56° S) by multi-mission satellite radar altimetry; canopy heights replaced by altimetry heights | H: WGS84 V: EGM96 | H: 3 arc sec × 3 arc sec (~90 m × 90 m) V: > 10 m | Smith and Berry (2009); (2010); Berry et al. (2019) | Free |
| ASTER | DSM | 83° N to 83° S | 01/03/2000 to 30/11/2013 | Correlation of optical stereo near infrared imagery | H: WGS84 V: EGM96 | H: 1 arc sec × 1 arc sec (~30 m × 30 m) V: 20 m (LE95), 10.20 m RMSE | Abrams et al. (2010); Tachikawa et al. (2011) | Free |
| AW3D30 (ALOS) | DSM | 80° N to 80° S | 24/01/2006 to 12/05/2011 | Resampling AW3D (5 m resolution, based on optical stereo panchromatic | H: WGS84 V: EGM96 | H: 1 arc sec × 1 arc sec (~30 m × 30 m) | Tadono et al. (2016) | Partially free |

| | | | | | | | | |
|--------------------------|------------|----------------|-----------------------------|------------------------------------------------------------------------------------------------------------------------------------------------------------------------------------------|------------------------|-----------------------------------------------------------------------------------------------------------------------------------|----------------------------------------|---------------------------|
| | | | | imagery) by applying average and medium methods | | V: 4.38 m (σ), 4.40 m RMSE | | |
| TanDEM-X 30 m | DSM | 90° N to 90° S | 12/12/2010 to 16/01/2015 | Bi-static Synthetic Aperture Radar interferometry (twin satellites) | H: WGS84 V: WGS84 | H: 1 arc sec \times 1 arc sec (~30 m \times 30 m) V: < 10 m (LE90) | Wessel (2018) | Free for scientific use |
| TanDEM-X 12 m | DSM | 90° N to 90° S | 12/12/2010 to 16/01/2015 | Bi-static Synthetic Aperture Radar interferometry (twin satellites) | H: WGS84 V: WGS84 | H: 0.4 arc sec \times 0.4 arc sec (~12 m \times 12 m); between 0° and 50° N/S V: < 10 (2–4) m (LE90), up to 6.78 m RMSE | Wessel (2018); Wessel et al. (2018) | Free for scientific use |
| Copernicus DEM GLO-30 | DSM | 90° N to 90° S | 12/12/2010 to 16/01/2015 | Correction of WorldDEM™ (source DEM) (based on TanDEM-X 12 m) by filling voids with ASTER, SRTM90, SRTM30; GMTED2010, SRTM30plus, TerraSAR-X Radargrammetric DEM, AW3D30, and Norway DEM | H: WGS84 V: EGM2008 | H: 1 arc sec \times 1 arc sec (~30 m \times 30 m); between 0° and 50° N/S V: < 4 (2–4) m (LE90) | Airbus Defence and Space (2020) | Free for registered users |
| FABDEM | nearly DTM | 90° N to 90° S | 12/12/2010 to 16/01/2015 | Correction of Copernicus DEM (source DEM) GLO-30 by removing buildings and forest height bias through machine learning techniques | H: WGS84 V: EGM2008 | H: 1 arc sec \times 1 arc sec (~30 m \times 30 m); between 0° and 50° N/S V: 2.39–6.67 m (LE90); 2.33–6.66 m (RMSE) | Hawker et al. (2022) | Free |

| | | | | | | | | |
|--------------------|-----|-------------------------------------------------------|-------------------------------------------------------------|--------------------------------------------------------------------------------------------------------------------------------------------------------------------------|-----------------------------------------------------|-----------------------------------------------------------------------------------------------------------------------------------------------------------------------------------------------|-------------------------------|----------------------------|
| CoastalDEM v2.1 | DTM | nearly input elevation between -10 and 120 m | 60° N to 56° S; 11/02/2000 to 22/02/2000 (source DEM) | Correction of NASADEM by training with ICESat 2 satellite LiDAR data and using additional population and vegetation datasets in a neural network | H: WGS84 V: EGM96 | H: 3 arc sec × 3 arc sec (~90 m × 90 m) V: 2.99–3.75 m (LE90; for maximum elevations of 5 to 20 m); 2.63– 3.23 m (RMSE; for maximum elevations of 5 to 20 m) | Kulp and Strauss (2021) | Free for scientific use |
| GLL-DTM v1 | DTM | 90° N to 90° S; input elevation < 10 m | 14/10/2018 to 13/05/2020 | Inverse distance interpolation of ICESat 2 satellite LiDAR data | H: WGS84 V: MSL | H: 0.05° × 0.05° (~5 km × 5 km) V: 0.50–0.54 m (RMSE; for maximum elevations of 2 to 10 m) | Vernimmen et al. (2020) | Free |
| AD-DEM | DTM | Ayeyarwady Delta; input elevation ≤ 10 m | 26/01/2002 to 10/04/2004 | Aerial photography, levelling, GPS observations and geodetic framework was conducted in 08/2000) | H: Everest 1830; Adjustment 1937 V: MSL | H: 750 m × 750 m (~0.007 × 0.07°) | This study | Free |

Shuttle Radar Topography Mission (SRTM) was a joint venture of NASA, the National Geospatial-Intelligence Agency and the German and Italian Space Agencies (Farr et al., 2007) that provides the first dataset of land elevation covering ca. 80 % of the Earth's land surfaces (NASA JPL, 2016). In February 2000, the data was acquired by two antennas mounted on the shuttle and an extendable mast in 60 m distance. Since the radar signal could not sufficiently penetrate canopies, the SRTM DEM 40 constitutes a digital surface model (DSM). The envisaged vertical accuracy of 16 m (linear error at 90 % confidence (LE90)) was achieved and is equivalent to < 10 m root mean square error (RMSE) (Rabus et al., 2003; Rodríguez et al., 2005; Farr et al., 2007; Mukul et al., 2017). However, as global and regional comparisons against ground truth data turned out spatially varying vertical accuracy, it was decided to improve the quality of the SRTM globally by integrating satellite radar altimetry

data from multiple missions to generate the Altimetry Corrected Elevations, Version 2, dataset (ACE2) (Table S1; Berry et al., 45 2010). In addition, GLOBE data was included to extend the original coverage area of SRTM to 60° S. After analysing waveforms of the entire geodetic mission, all accepted ones were retracked and fused with orbit data and the EGM96 geoid model (Lemoine et al., 1997) to refer to orthometric heights (Berry et al., 2010). From available spatial resolutions of 3, 9 and 30 arc seconds, we obtained data at the highest resolution of 3 arc sec (~90 m). While vertical errors still exceed 10 m (Table S1; Smith and Berry, 2009), the effective penetration of canopies by the altimeter signal, which is reflected by the ground, is 50 responsible for the significant differences between the SRTM and ACE2 that have been documented particularly for tropical rain forests (Smith and Berry, 2009). However, being merged with the SRTM dataset, the ACE2 should not be regarded as a thorough DTM. While water body data is available for the SRTM, distinguishing water from land by two classes, additional datasets for ACE2 include a source, quality, and confidence matrices (Smith and Berry, 2009).

In contrast to these DEMs, the Advanced Spaceborne Thermal Emission and Reflection Radiometer (ASTER) Global Digital 55 Elevation Model (GDEM) Version 3 (ASTGTM) is based on optical stereo imagery acquired by the ASTER instrument (Yamaguchi et al., 1998) mounted on NASA's Terra satellite which was launched in 1999 (Abrams et al., 2020). Version 3 (published in 2019; Abrams et al., 2020) includes 200,000 additional scenes to supplement and fill data gaps of previous versions and has been processed by applying anomaly corrections and void filling with data from ASTER GDEM version 2, SRTM (processed for NASADEM), and ALOS World 3D-30m (AW3D30) (Abrams and Crippen, 2019). Both datums and 60 resolutions are similar to SRTM. Vertical accuracy, which is 20 m (LE95) and 10.20 m RMSE for version 1 (Ministry of Economy, Trade and Industry (METI) of Japan et al., 2009), has been documented to improve significantly towards version 2 while only minor further improvements have been observed towards version 3 (e.g., Tachikawa et al., 2011; Abrams and Crippen, 2019; Talchabhadel et al., 2021; Altunel et al., 2022). Along with the ASTER GDEM version 3 (ASTGTM), the ASTER Water Body Dataset (ASTWBD) was published, subdividing water bodies into ocean, river, and lake classes (Abrams 65 et al., 2020).

Similar to ASTER, the ALOS World 3D 30 m mesh (AW3D30) constitutes a DSM originating from optical data, that was acquired by using the Panchromatic Remote sensing Instrument for Stereo Mapping (PRISM) of the Advanced Land Observing Satellite (ALOS) operated by the Japan Aerospace Exploration Agency (JAXA) (Tadono et al., 2016). Using ortho-rectified PRISM imagery of 2.5 m spatial resolution, the AW3D DSM (5 m spatial resolution) was generated (Takaku et al., 2014) and 70 subsequently resampled by applying averaging and selecting medium heights, respectively (Tadono et al., 2016). Absolute vertical accuracy was determined for more than 5,000 ground control points spread over 127 DEM tiles and revealed errors of ~4.40 m, which is below the targeted 5 m mark (Table S1; Tadono et al., 2016). Available additional datasets related to the AW3D30 include a mask file, distinguishing between sea and inland water bodies (JAXA, 2019), a stacking number file, header, and quality assurance information files, as well as a list file for versions 2.1 and 2.2 (JAXA, 2019).

75 Covering more than 150 million km² (German Aerospace Centre (DLR), 2013), the TanDEM-X provides elevation data for the entire land surface of the Earth (Table S1). The DEM was generated based on interferometric synthetic aperture radar (SAR) data acquired by the twin satellite constellation of TerraSAR-X and TanDEM-X (Krieger et al., 2007; Wessel, 2018).

DEM tiles of 12 m and 30 m spatial resolution can be accessed via the DLR website after submitting a proposal and are free of charge for scientific use. In contrast to the DEMs mentioned before, elevations of the TanDEM-X are given in ellipsoidal heights. Absolute vertical accuracy is less than 10 m (LE90; Wessel, 2018) while relative accuracy has been estimated at least for the TanDEM-X 12 m data and ranges from 2 m (for slopes $\leq 20\%$) to 4 m (for slopes $> 20\%$; Rizzoli et al., 2017; Wessel, 2018). In addition, investigations on the terrain of selected test sites revealed RMSEs of up to 6.78 m (Wessel et al., 2018). To ensure transparency and enable detailed investigations of the dataset by the user, each TanDEM-X tile is provided in conjunction with a set of information layers, including, amongst others, a height error map, a water indication mask based on amplitude and coherence information (Wendleter et al., 2012), a coverage map as well as a layover and shadow mask (Wessel, 2018). Moreover, the TanDEM-X 12 m data of DLR were edited by Airbus Defence and Space to provide the so called WorldDEM in different versions to commercial users, including, amongst other improvements, the transformation from ellipsoidal to orthometric heights (Airbus Defence and Space, 2018). To further improve the performance of the DEM, Airbus used the WorldDEMTM version, where implausible terrain features and water bodies have been edited and controlled by a quality check (Airbus Defence and Space, 2018). Based on the WorldDEMTM, Airbus Defence and Space (2020) generated several quality layers that provide auxiliary information and were published together with the DEM as the Copernicus DEM in 2021 (Airbus Defence and Space, 2020). Improvements include, for example, void filling with elevation data of ASTER, different versions of SRTM, GMTED2010, TerraSAR-X Radargrammetric DEM, AW3D30, and Norway DEM (Airbus Defence and Space, 2020). Thus, absolute vertical accuracy improved to < 4 m compared to the TanDEM-X 12 m (Table S1) and recent publications recommend its use over previous global DEMs (Guth and Geoffroy, 2021; Marešová et al., 2021). From available 10 m, 30 m, and 90 m spatial resolutions of Copernicus DEM, we used the 30 m version. The water body mask that is provided by Airbus Defence and Space (2020) allows for separating ocean, lakes, and rivers.

The most recently published global DEM is the so called Forest And Buildings removed Copernicus DEM (FABDEM) of Hawker et al. (2022). Using a three step correction workflow including forest and building predictor data, random forest machine learning models, and post-processing, they eliminated the bias of tree and building heights in the Copernicus DEM GLO-30 (Hawker et al., 2022), thereby providing nearly terrain elevation. Vertical errors of the Copernicus DEM were reduced from 2.87 to 2.33 m RMSE (1.61 to 1.12 m mean absolute error (MAE)) for urban areas and from 7.98 to 4.96 m RMSE (5.15 to 2.88 m MAE) for forest areas (Hawker et al., 2022).

In contrast to these global DEMs generated for being used in various applications, the CoastalDEM (Kulp and Strauss, 2018; Kulp and Strauss, 2021) and the Global LiDAR lowland DTM (GLL-DTM v1; Vernimmen et al., 2020) aim at improving studies of SLR, flooding, and vulnerability in coastal settings (Kulp and Strauss, 2018; Kulp and Strauss, 2019; Vernimmen et al., 2020; Hooijer and Vernimmen, 2021; Kulp and Strauss, 2021). In 2018, Kulp and Strauss (2018) published their first version of the CoastalDEM, which included 23 variables and is based on SRTM elevation data trained with airborne LiDAR elevation data from the United States and Australia in a multilayer perceptron neural network. Though elevation bias could be reduced for test sites in the United States and Australia, the CoastalDEM v1.1 was likely overfitted as comparisons with other global and local DEMs for study areas like the Mekong Delta show (Vernimmen et al., 2020). Therefore, Kulp and Strauss

(2021) revised the CoastalDEM by updating source elevation data with the recently published NASADEM (i.e., an improved SRTM; Buckley et al., 2020), using global ICESat 2 satellite LiDAR data for training, and including new and updated input variables in a convolutional neural network (Table S1; Kulp and Strauss, 2021). Thus, for maximum elevations of 5 m (20 m),
115 LE90 improved from 4.24 m (5.73 m) of CoastalDEM v1.1 to 2.99 m (3.75 m) of CoastalDEM v2.1, which is equivalent to reduced RMSE of 4.02 m (4.83 m) in v1.1 and 2.63 m (3.23 m) in v2.1 (Kulp and Strauss, 2021).

Instead of using ICESat 2 data for training, Vernimmen et al. (2020) interpolated the ground track data themselves into a DEM (Table S1). However, due to the setup of the satellite LiDAR with ~90 m across-track distance within beam pairs and along-track distance of ~ 2.5 km (Neuenschwander et al., 2021), horizontal accuracy of the GLL-DTM is much less than for other
120 global DEMs (Table S1) but will likely be improved in future versions as the number of ICESat 2 recordings increases (Vernimmen et al., 2020). The dataset is referenced to MSL based on Mean Dynamic Topography (MDT) data of Rio et al. (2014) and yields vertical accuracies of 0.54 m RMSE for coastal lowland < 10 m (Table S1; Vernimmen et al., 2020).

S1.1.3. Mean Dynamic Topography

In the absence of available information on local MSL in Myanmar and its potential offset to a geoid reference, we used MDT
125 data as an estimation of sea surface height in relation to geoid. Furthermore, it may provide a more steady and reliable reference given the spatial and temporal variability of tidal range.

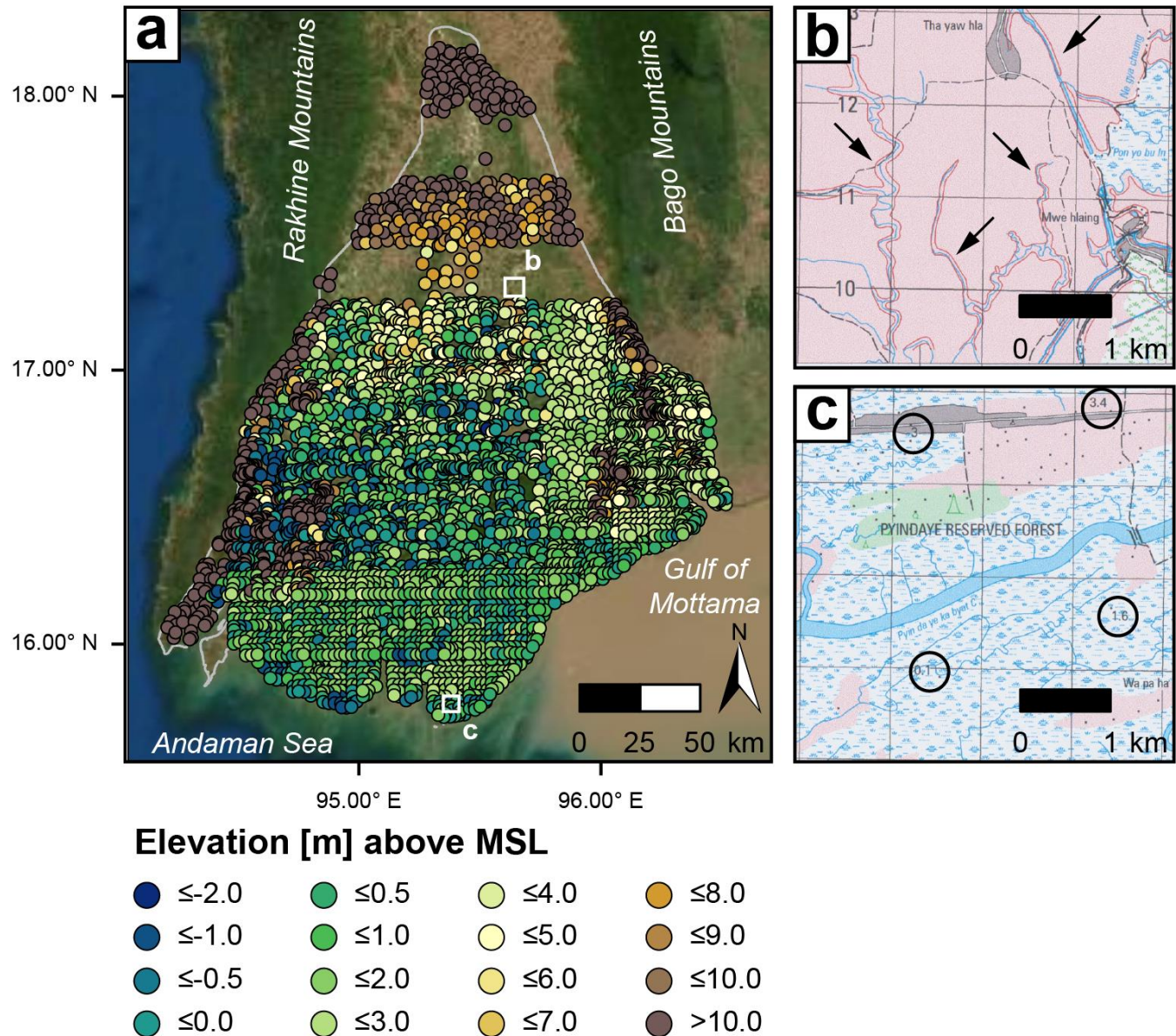
The latest MDT, i.e. the CNES-CLS18 dataset of Mulet et al. (2021), was used and accessed via the AVISO+ website (<https://www.aviso.altimetry.fr/en/data/products/auxiliary-products/mdt/mdt-global-cnes-cls18.html>, last access: 22 February 2022). Compared to previous MDT data, the MDT CNES-CLS18 dataset (from now on referred to only as MDT) combines
130 extended records of altimetry and gravitational field measurements as well as in situ oceanographic data from drifting buoys and hydrological profiles and thereby provides estimates on mean sea surface heights at higher spatial resolution (i.e., 0.125°) with improvements particularly for coastal areas and ocean surface currents (Mulet et al., 2021; AVISO+, 2022). As the MDT is a global dataset covering all ocean surfaces of the Earth, it allows us to account for potential sea level variations along the
135 Myanmar coast, especially from the delta towards Kyaikkhami at the Tanintharyi coast in the east and thus to apply a continuous MSL correction instead of using one single reference tide gauge. However, since the MDT is referenced to GOCO05s geoid (Mayer-Gürr et al., 2015), thereby differing from vertical datums of the DEMs, requires investigations of geoid/ellipsoid height anomalies prior to converting the DEMs to MSL.

S1.2. Processing

S1.2.1. Generation of an elevation model for the Ayeyarwady Delta based on geodetic data

140 To create a local DEM for our region of interest (ROI; the spatial extent of the Ayeyarwady Delta as defined by Tessler et al. (2015)), 102 map sheets were georeferenced and digitised, covering also the wider surroundings (15° 30' N to 18° 30' N and 94° 0' E to 97° 0' E) to enhance the performance of DEM interpolation. In total, 9179 elevation points were digitised (5,673

lying within the ROI). These include also relative heights (e.g., in case of dam slopes) and benchmarks but given the absence of any documentation on their absolute elevation reduced the dataset to 8,145 spot heights (4,792 within the ROI). Albeit there
145 are no significant differences between horizontal datums of the WGS84 and Everest 1830 ellipsoids, the digitised elevation data were projected to UTM 46 N based on the Everest 1830 ellipsoid to refer, besides the vertical reference, also to a common horizontal datum and UTM zone, consistent with the Myanmar 2000 datum (JICA et al., 2004b). Given unsystematically distributed point elevations and data gaps especially in the northern delta parts (Fig. S1), contour lines of these areas were
150 digitised with points extracted at 250 m and 2000 m intervals, respectively, to supplement the input elevation data for DEM interpolations and testing the impact of considering contour data in DEM interpolation. Furthermore, to reduce the potential of height overestimations in the immediate surroundings of outcrops and improve the quality of the DEM in low lying coastal areas, which are of particular interest in this study, values of elevation higher than a specific threshold are excluded, thereby eliminating outcrops.



155

Fig. S1. Spot heights from topographic maps used for interpolation of the AD-DEM (a; contour data are not shown). The spot heights in the north of the delta are irregularly distributed and do not provide full spatial coverage. In these parts, topographic information is only provided by contour lines along the river banks (marked with black arrows; b). The spot heights (marked with black circles; c) provide full spatial coverage and a more regular pattern in the southern, central part of the delta. a) is based on Esri World Imagery (2017); b) and c) are based on topographical map sheets 4143-4 (b) and 4040-1 (c) from East View Geospatial, Inc. (2014).

Interpolation was conducted using the Geostatistical Wizard within the Analysis environment of ArcGIS Pro 2.9.1. Minderhoud et al. (2019) compared 22 interpolation methods for the creation of a DEM in a similar setting, i.e., the Mekong Delta, and found Empirical Bayesian Kriging with empirical transformation and exponential modelling providing the most accurate results (i.e., in terms of absolute accuracy), similar set-up settings were adopted in this study. The grid cell resolution was defined as justified by the point density following Aguilar et al. (2006). In total, nine versions of AD-DEM were generated – (i–iii) including digitised spot heights, (iv–vi) including spot heights and contour heights extracted every 250 m, and (vii–ix) including spot heights and contour heights extracted every 2000 m. All of them apply also specific elevation thresholds of 20 m and 10 m, respectively (Table S2). Areas – such as outcrops and northernmost delta parts – that are in reality higher than the elevation threshold applied for DEM interpolation were masked. As data collection for generating the topographic maps used for the AD-DEM was conducted between 2002 and 2004, the location of river channels is most likely best reflected by the SRTM water body mask created in 2000 as changes in geomorphology following river meandering and channel migration will be less compared to water masks of DEMs generated at a later point in time. Therefore, we used the SRTM water body mask file (NASA JPL, 2013) to exclude all areas marked as water from the final DEMs.

S1.2.2. Processing of global DEMs and determination of local mean sea level (MSL)

Pre-processing of global DEMs and their respective water mask files included mosaicking of single DEM tiles, re-projection to UTM 46 N based on Everest 1830 ellipsoid, and clipping to the ROI. The variety of vertical datums used by the array of DEMs together with the complex geoid setting along the Myanmar coast made datum transformation to MSL challenging as relations between vertical references of MDT and DEM data need to be considered when correcting from geoid to MSL (Fig. 2). Processing involved in total three datum conversions. First, given that the majority of DEMs is referenced to the EGM96 geoid, the other datasets were transformed to EGM96 as well. Second, the original MDT data (called $MDT_{GOCO05s}$) was transposed to EGM96 (called MDT_{EGM96}). Given the general relationship of geoid and sea level according to Eq. (1):

$$N_{GOCO05s} + MDT_{GOCO05s} = N_{EGM96} + MDT_{EGM96}, \quad (1)$$

where N_{EGM96} and $N_{GOCO05s}$ are the respective height anomalies in relation to the reference ellipsoid WGS84, $MDT_{GOCO05s}$ is the original MDT data that needs to be transposed to EGM96, hereafter referred to as MDT_{EGM96} , Eq. (2) denotes the term of datum conversion of the MDT from GOCO05s to EGM96:

$$MDT_{EGM96} = MDT_{GOCO05s} + (N_{GOCO05s} - N_{EGM96}). \quad (2)$$

Subsequently, the third datum conversion was conducted by applying the MDT_{EGM96} to correct the DEMs to MSL. To transform the MDT of Mulet et al. (2021) from GOCO05s to EGM96, the offset between these two geoids was determined by using height anomaly to the reference ellipsoid WGS84. Height anomalies at 0.2° spatial resolution were obtained from the online ICGEM calculation service provided by the German Research Centre for Geosciences (GFZ; Ince et al., 2019). Compared to all other interpolation methods available in the geostatistical wizard of ArcGIS Pro, multiquadric radial basis

functions revealed smallest RMSE, have been recommended also by other studies focussing on gravitational field modelling
195 (Doganalp and Selvi, 2015; Li, 2018 and references therein), and were thus chosen to interpolate geoid height anomalies from point to raster. Overall negative height anomalies indicate the location of both geoids below the WGS84 ellipsoid and show repeated crossings along the Ayeyarwady Delta and Tanintharyi coasts, thus underpinning the use of a continuous MSL correction instead of referring to a single reference site (Fig. S2). The offset between the two geoids was determined by subtracting the EGM96 from the GOCO05s data (Fig. 2; Eq. (1)).

200

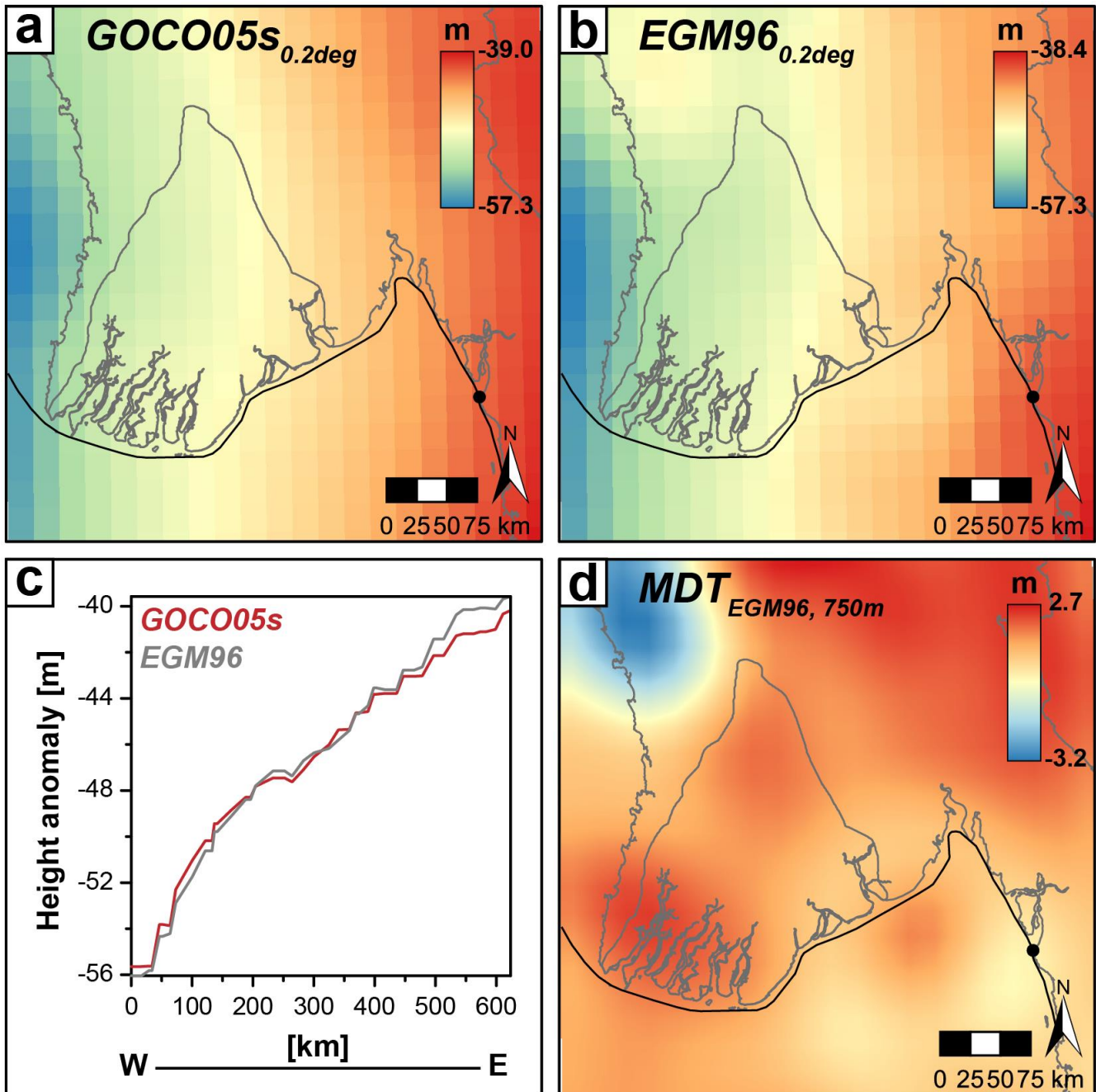


Fig. S2. Regional setting of geoids (a–c) relevant to transpose MDT data from GOCO05s to EGM96 geoid (d).

Height anomalies of GOCO05s and EGM96 compared to WGS84 ellipsoid (a and b) and compared to each other along a shoreline profile (black line; a–c). Processing of the MDT resulted in a MDT dataset, which is referenced to EGM96 geoid and resampled to a spatial resolution of 750 m (d). The black dot at the Tanintharyi coast shows the location of Kyaikkhami, where the original vertical basis of Myanmar elevation data is located.

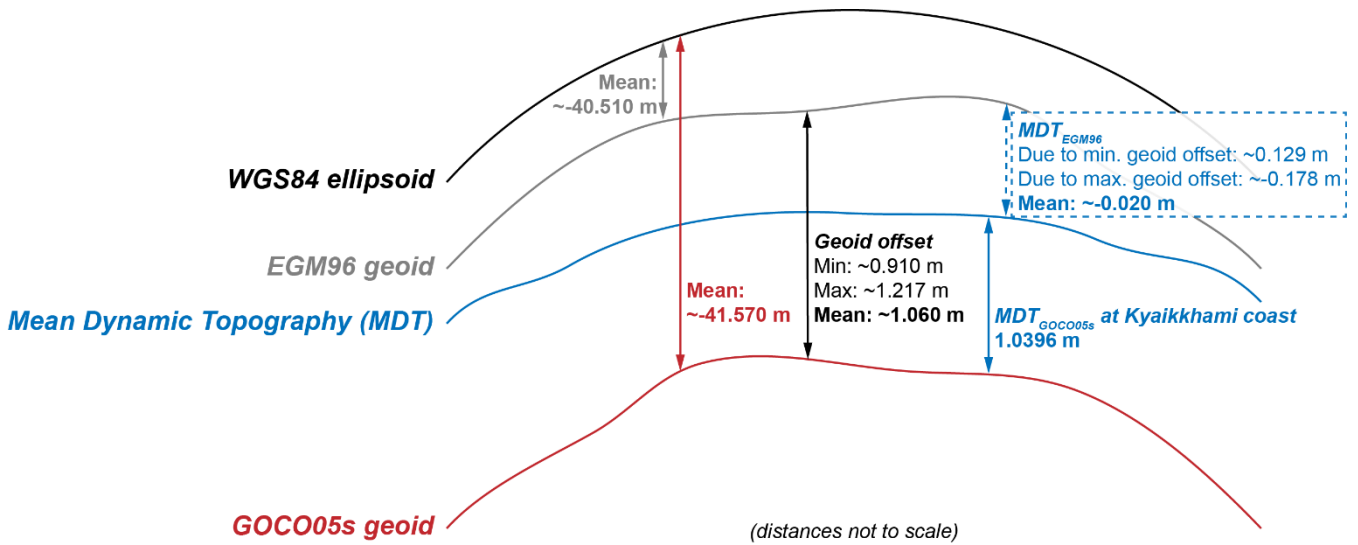


Fig. S3. Relations between Mean Dynamic Topography (MDT) and EGM96 and GOCO05s geoids with respect to WGS84 ellipsoid for the coastal area of Kyaikkhami in Myanmar (distances are not to scale).

To transpose the AD-DEM from local MSL at Kyaikkhami to a continuous local MSL (based on MDT_{EGM96}), first the difference between the vertical reference of the AD-DEM (i.e., MSL at Kyaikkhami) and EGM96 needs to be determined.

Based on the original resolution of the MDT data (0.125°), this offset is only ~ 0.02 m and hardly ~ 0.01 m if the resampled MDT (750 m spatial resolution) is used. Therefore, the vertical reference of the AD-DEM can be converted to the continuous sea level directly, without prior transposition of the elevation data to EGM96.

Before adding the offset to the $MDT_{GOCO05s}$ data to transpose it to EGM96 according to Eq. (2), extrapolation over land is required to enable calculation of MDT with elevation data. For this, points were created from the $MDT_{GOCO05s}$ raster and interpolated over land. The decision whether to use IDW interpolation or Empirical Bayesian Kriging was made based on the point comparison of input and output data at identical locations. Residuals are almost absent for both interpolation algorithms. Finally, inverse distance weighting (IDW, with a power of 2) was used for interpolating the MDT data as it takes the closest value along the coast for extrapolation over land (see also Vernimmen et al., 2020). Finally, the resolution of the processed MDT_{EGM96} was resampled to match the resolution of the AD-DEM using bilinear interpolation.

For converting vertical datums of the DEMs, we first transformed tiles of TanDEM-X, Copernicus DEM, and FABDEM to EGM96 geoid (15 min resolution) prior to mosaicking using the elevation recalculation raster function in ERDAS Imagine 2020 software environment. It should be noted that since the GLL-DTM v1 of Vernimmen et al. (2020) was already referenced to MSL, this DEM did not require the processing as outlined in Fig. 2. However, the GLL-DTM v1 refers to MSL based on an older MDT dataset (Rio et al., 2014), which is referenced to the EGM-DIR-R4 geoid, where the potential offset between this geoid and the original geoid reference of DEM data was not considered. Without the MDT interpolation over land of

230 Vernimmen et al. (2020), undoing their MSL referencing to MDT of Rio et al. (2014) and applying our MDT correction would introduce additional bias and thus seems not meaningful. Due to the missing integration of geoid offset, the GLL-DTM v1 should be used with caution. Although we are unable to correct the GLL-DTM v1 ourselves, we included it into our investigations of the Ayeyarwady Delta as it was generated especially for coastal lowlands and to highlight the importance of carefully dealing with vertical datums of datasets using different geoid models.

235 Prior to transformation of the AD-DEM from its original reference (i.e., local MSL at Kyaikkhami) to the continuous MSL of the MDT_{EGM96}, the offset of MSL Kyaikkhami to EGM96 was determined. According to MDT_{EGM96}, MSL at Kyaikkhami is nearly identical with the EGM96 geoid height with offsets of ~0.02 m (0.125° resolution) and ~0.01 m (750 m resolution; Fig. S3). Though the accuracy of MDT data has been improved to centimetre scale since the launch of the GOCE satellite in 2009 (Knudsen et al., 2011), comparisons of latest MDT datasets with independent MDT data and tide gauges document regional 240 deviations of up to ~10 cm (Hamden et al., 2021), thus exceeding the offset of Kyaikkhami MSL to EGM96. Therefore, we did not correct for the local geoid offset in Kyaikkhami but converted the vertical reference of the AD-DEM to MSL in the delta directly by subtracting MDT_{EGM96}, without prior transposition of elevation data to EGM96. Against the background that geoid omission errors and commission errors of both geoid and mean sea surface data constitute the total error of satellite-based MDT data (Bingham et al., 2014; Andersen et al., 2018), it should be kept in mind that uncertainties remain particularly 245 for coastal zones as altimetric monitoring and geoid mapping are influenced by the more pronounced coastal topography/bathymetry compared to off-shore as well as coastal MDT dynamics (Andersen et al., 2018; Filmer et al., 2018). After referencing the DEMs to MSL, inland water bodies were masked using the DEM-specific water mask files. In addition, cell values with an elevation of more than 7 m below MSL were removed as they likely constitute erroneous height estimates, following Vernimmen et al. (2020) who refer to the lowest point of the Netherlands located in the Zuidplaspolder (e.g., de 250 Groot-Reichwein et al., 2014). Depending on the type of validation, i.e., with spot heights from topographic maps (East View Geospatial, Inc., 2014) or the AD-DEM, the global DEMs were further processed. The spatial resolution of the DEMs was resampled to match comparably the horizontal accuracy of the AD-DEM using the bilinear resampling technique. For validating the GLL-DTM v1, the AD-DEM was resampled to its resolution of 0.05° (Table S1). Since outcrops and elevation values outside critical lowlands have been excluded to improve the interpolation of the AD-DEM, these areas were also 255 excluded in the global DEMs to ensure comparability among all DEMs of this study.

S1.2.3. Mapping of areas prone to monsoon flooding

Besides direct validation using spot heights and the AD-DEM, we also performed an additional validation of relative elevation for the DEMs by their ability to match observed floods in deltaic areas affected by inland flooding. We adopted the principal approach from Minderhoud et al. (2019) who used the correlation of land elevation and tidal flooding to assess the quality of 260 DEMs indirectly. Here, we use mappings of recent monsoon floods due to increased discharge as this allows for investigating the relation between topography and flood pattern also inland. Therefore, we mapped areas inundated during the monsoon periods of 2015 and 2020, respectively, using an image rationing change detection approach on Sentinel 1 imagery (10 m

spatial resolution) in the environment of Google Earth Engine (GEE; Gorelick et al., 2017). The pre-event imagery was recorded in February during the dry season while the selection of imagery capturing maximum flood extents was made based 265 on investigations of rainfall amounts and river discharge. Monthly accumulated precipitation estimates were obtained from the GPM_3IMERGM v6 product of NASA Global Precipitation Measurement (GPM) program (Huffman et al., 2019) for the rainy months from May to October via the NASA Giovanni web environment (NASA, 2021). Discharge estimates from satellite microwave radiometry were accessed via the River and Reservoir Watch Version 4.5 processor of the Dartmouth 270 Flood Observatory (Brakenridge et al., 2022) and were downloaded for River Watch stations 25, 29, and 30. Since an array of GEE scripts has been published in the recent past (e.g., Inman and Lyons, 2020; Peter et al., 2020; Mehmood et al., 2021; Moharrami et al., 2021; Tripathy and Malladi, 2022), we adopted the script of United Nations Platform for Space-based Information for Disaster Management and Emergency Response (UN-SPIDER 2019) and slightly adjusted it, i.e., by setting the difference threshold to 1.3, thereby minimising false positive and false negative detections. For further handling and analysis, the data was vectorised in the ArcGIS Pro environment.

275 **S2. Results and interpretation**

S2.1. Performance and accuracy of the AD-DEM

Table S2. Summary of cross validation measures for all nine versions of the AD-DEM from the Empirical Bayesian Kriging algorithm.

To ensure data accuracy as good as possible, especially in data sparse and low lying delta parts, DEM interpolation was 280 conducted by integrating spot heights and points extracted from contour lines in 250 m and 2000 m intervals, respectively, as well as by excluding elevations > 20 m and > 10 m. Since the AD-DEM, which was generated based on spot heights and points taken from contour lines in a 250 m interval, both ≤ 10 m, reveals the lowest error statistics, this version (in italics) was used for assessing the performance of common global and coastal DEMs.

| | AD-DEM_i | AD-DEM_{ii} | AD-DEM_{iii} | AD-DEM_{iv} | AD-DEM_v | AD-DEM_{vi} | AD-DEM_{vii} | AD-DEM_{viii} | AD-DEM_{ix} |
|--------------------------------------|---------------------------|----------------------------|-----------------------------|----------------------------|---------------------------|----------------------------|-----------------------------|------------------------------|----------------------------|
| Contour points interval | - | - | - | 250 m | 250 m | 250 m | 2000 m | 2000 m | 2000 m |
| Integrated elevation threshold | - | ≤ 20 m | ≤ 10 m | - | ≤ 20 m | ≤ 10 m | - | ≤ 20 m | ≤ 10 m |
| N (spot heights) | 8145 | 5666 | 5108 | 8145 | 5666 | <i>5108</i> | 8145 | 5666 | 5108 |
| N (contour points) | - | - | - | 22791 | 20580 | <i>13582</i> | 2068 | 1841 | 1205 |
| Mean (prediction error) | 0.110 | -0.028 | -0.008 | -0.044 | 0.040 | <i>0.025</i> | 0.017 | -0.003 | 0.005 |
| Mean (prediction error) standardised | 0.015 | 0.003 | -0.003 | Not a number | Not a number | <i>Not a number</i> | 0.008 | 0.003 | Not a number |

| | | | | | | | | | |
|---------------------------|--------|--------|--------|-----------------|-----------------|-------------------------|--------|-------|-----------------|
| RMSE | 41.682 | 2.104 | 1.221 | 21.749 | 1.454 | <i>1.004</i> | 38.040 | 2.013 | 1.226 |
| RMSE standardised | 0.936 | 0.970 | 0.987 | Not a number | Not a number | <i>Not a number</i> | 1.129 | 1.037 | Not a number |
| Average standard error | 39.260 | 2.174 | 1.221 | 20.125 | 1.352 | <i>0.864</i> | 36.475 | 2.015 | 1.177 |
| Inside 90 % interval | 91.381 | 91.264 | 90.290 | 95.009 | 96.079 | <i>96.426</i> | 91.687 | 91.45 | 91.589 |
| Inside 95 % interval | 95.838 | 95.747 | 95.419 | 97.062 | 97.706 | <i>97.790</i> | 95.457 | 95.19 | 95.121 |
| Average CRPS | 9.519 | 0.882 | 0.619 | 2.923 | 0.353 | <i>0.251</i> | 8.017 | 0.783 | 0.547 |

285 **S2.2. Performance and accuracy of global satellite based DEMs**

S2.2.1. Performance of global DEMs based on visual impression

Table S3. Raster statistics for DEMs of this study. All DEMs were referenced to MSL. Elevations < -7.00 m above MSL and outcrops were excluded. Note that the GLL-DTM v1 refers to a different MDT dataset than used in this study, and without being corrected for geoid offset.

| DEM | Resolution (m) | N | Min (m) | Max (m) | Mean (m) | Median (m) | σ (m) |
|-----------------|----------------|-----------|---------|---------|----------|------------|--------------|
| SRTM | 30 | 27134565 | -7.00 | 72.18 | 4.69 | 3.90 | 3.36 |
| ACE2 | 90 | 11306350 | -7.00 | 43.91 | 1.68 | 0.94 | 3.13 |
| ASTGTM v003 | 30 | 27098350 | -2.21 | 90.88 | 6.99 | 6.32 | 3.50 |
| AW3D30 | 30 | 27152171 | -7.00 | 158.10 | 4.36 | 3.68 | 3.05 |
| TanDEM-X 30 m | 30 | 26808299 | -7.00 | 402.91 | 3.06 | 2.01 | 3.17 |
| TanDEM-X 12 m | 12 | 167583275 | -7.00 | 469.41 | 3.08 | 2.00 | 3.29 |
| Copernicus DEM | 30 | 26193614 | -6.88 | 48.65 | 3.04 | 1.99 | 3.06 |
| FABDEM | 30 | 26193621 | -1.84 | 45.59 | 2.75 | 1.83 | 2.59 |
| CoastalDEM v2.1 | 90 | 3032777 | -7.00 | 36.05 | 2.24 | 1.38 | 2.40 |
| GLL-DTM v1 | ~5889 | 633 | 0.31 | 9.88 | 2.62 | 2.07 | 1.75 |
| AD-DEM | ~5889 | 713 | -1.62 | 8.69 | 2.07 | 1.33 | 2.39 |
| AD-DEM | 750 | 45075 | -1.72 | 8.80 | 2.08 | 1.28 | 2.42 |

290

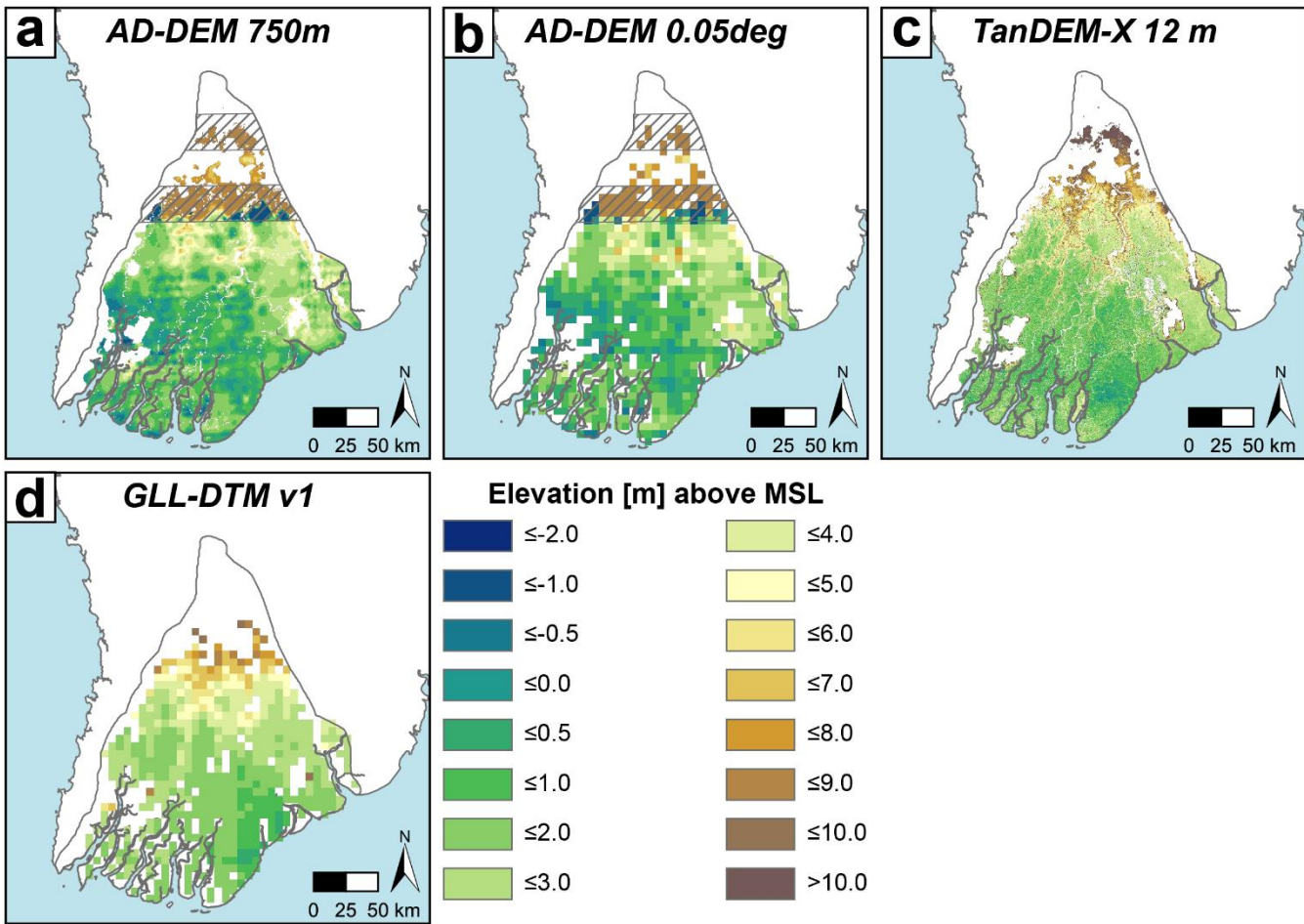
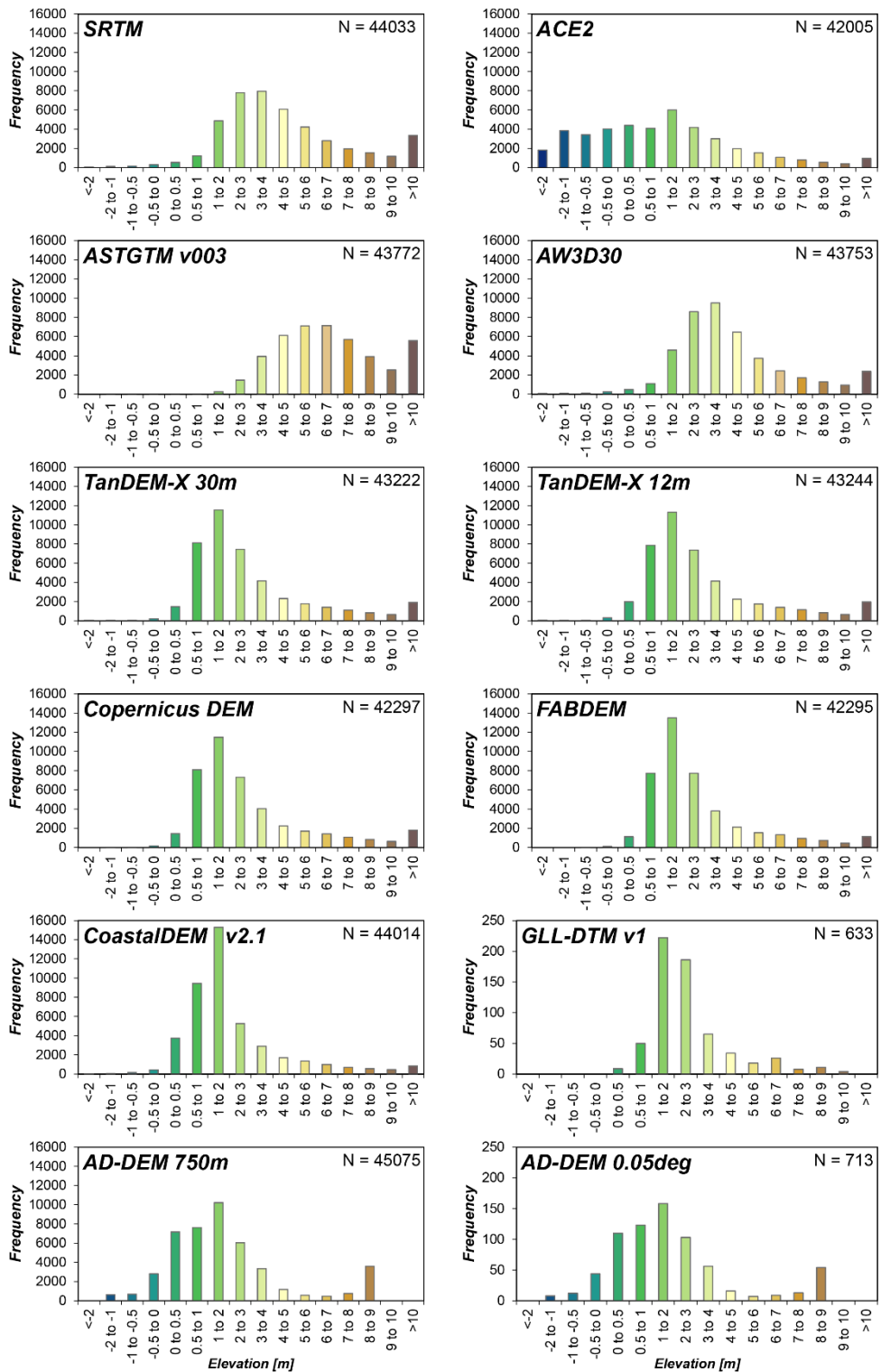


Fig. S4. The new local AD-DEM (a and b) in comparison to global digital elevation models in the Ayeyarwady Delta, which were excluded from the main text (c and d). Areas where AD-DEM has interpolation artefacts are hashed.



S2.2.2. Direct validation with spot heights from topographic maps

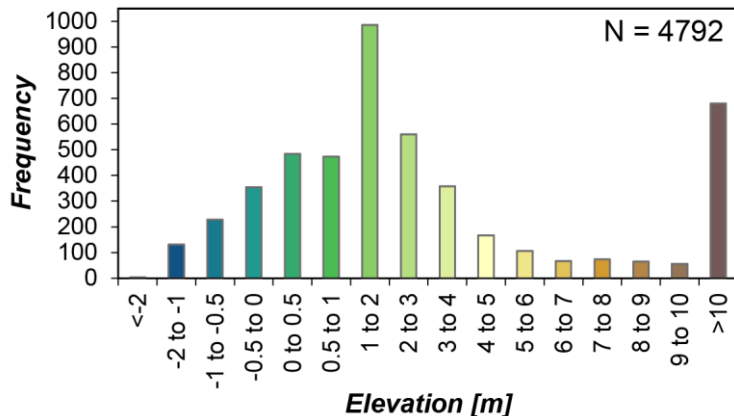


Fig. S6. Frequency distribution of elevation counts (in m) for spot heights inside the ROI of the Ayeyarwady Delta.

300

Table S4. Statistics for DEMs minus spot height elevation at spot height location. Best performances are shown in italics. DEMs were used in their original resolution. Since the GLL-DTM v1 is only valid for the low elevation coastal zone, it is excluded from validation with all spot heights. All DEMs were referenced to the same mean sea level. N – Number of spot heights in the ROI, with no data values excluded for each DEM respectively; HR – Height residual; MAE – Mean absolute error; RMSE – Root mean square error; Min – minimum DEM elevation at spot height location; Max – maximum DEM elevation at spot height location; Mean spot – mean elevation of all spot heights included in the comparison; Mean DEM – mean DEM elevation at all spot height locations included in the comparison; Median spot – median elevation of all spot heights included in the comparison; Median DEM – median DEM elevation at all spot height locations included in the comparison; σ spot – standard deviation of elevation of all spot heights included in the comparison; σ DEM – standard deviation of DEM elevation at all spot height locations included in the comparison; σ HR – standard deviation of height residuals; R^2 – Coefficient of determination.

| DEM | N | Mean | MAE | RMSE | Min | Max | Mean | Mean | Median | Median | Median | σ | σ | σ | R^2 |
|----------|------|-------|------|------|-------|--------|------|------|--------|--------|--------|----------|----------|----------|-------|
| | | HR | | | DEM | DEM | spot | DEM | spot | DEM | HR | spot | DEM | HR | |
| | | | | | | | | | | | | | | | |
| TanDEM-X | 4654 | -0.19 | 3.16 | 7.61 | -4.74 | 161.44 | 6.12 | 5.93 | 1.72 | 2.38 | 0.52 | 16.30 | 11.76 | 7.61 | 0.82 |
| 12 m | | | | | | | | | | | | | | | |

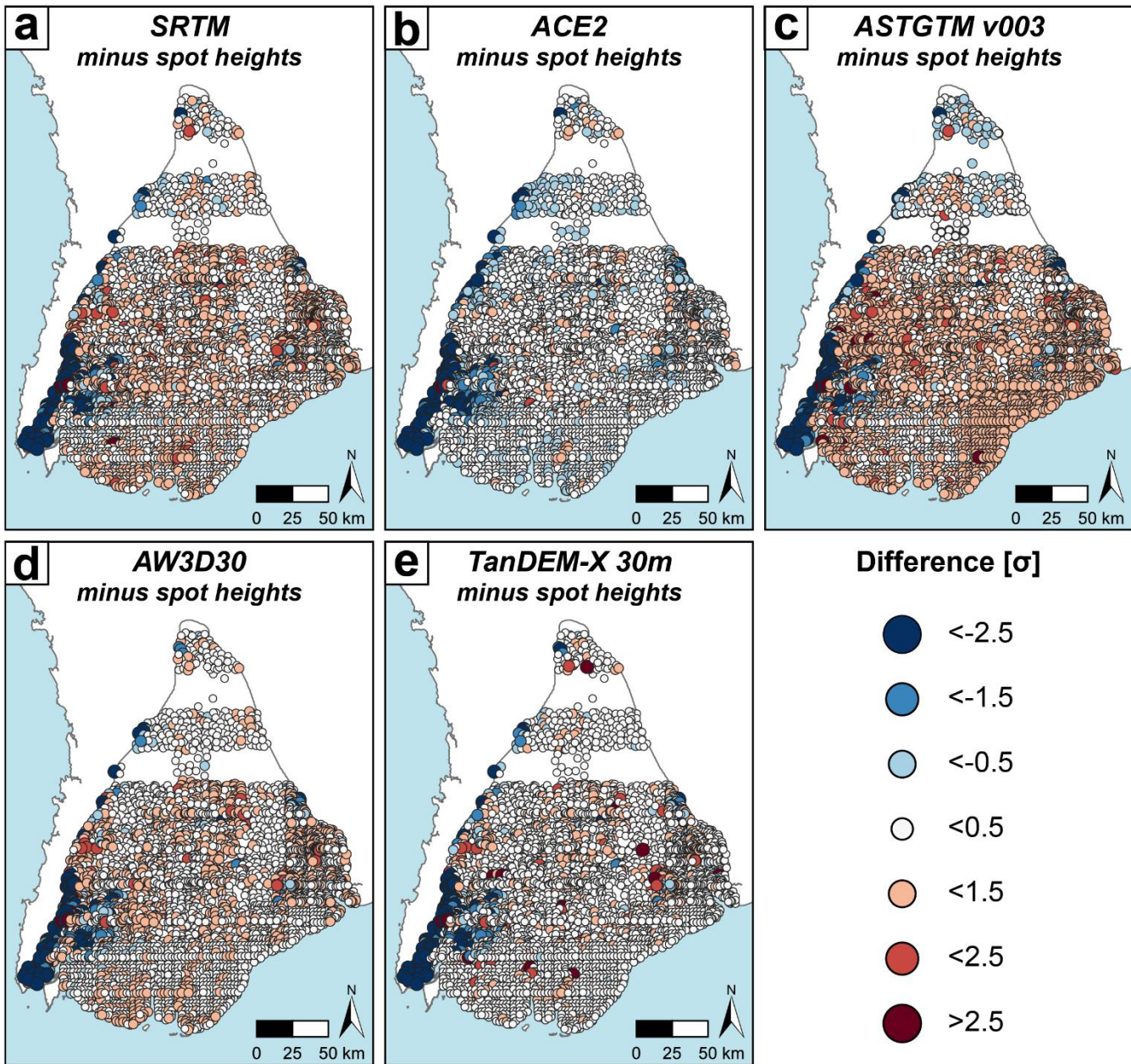


Fig. S7. Spot height residuals for global DEMs classified by standard deviation.

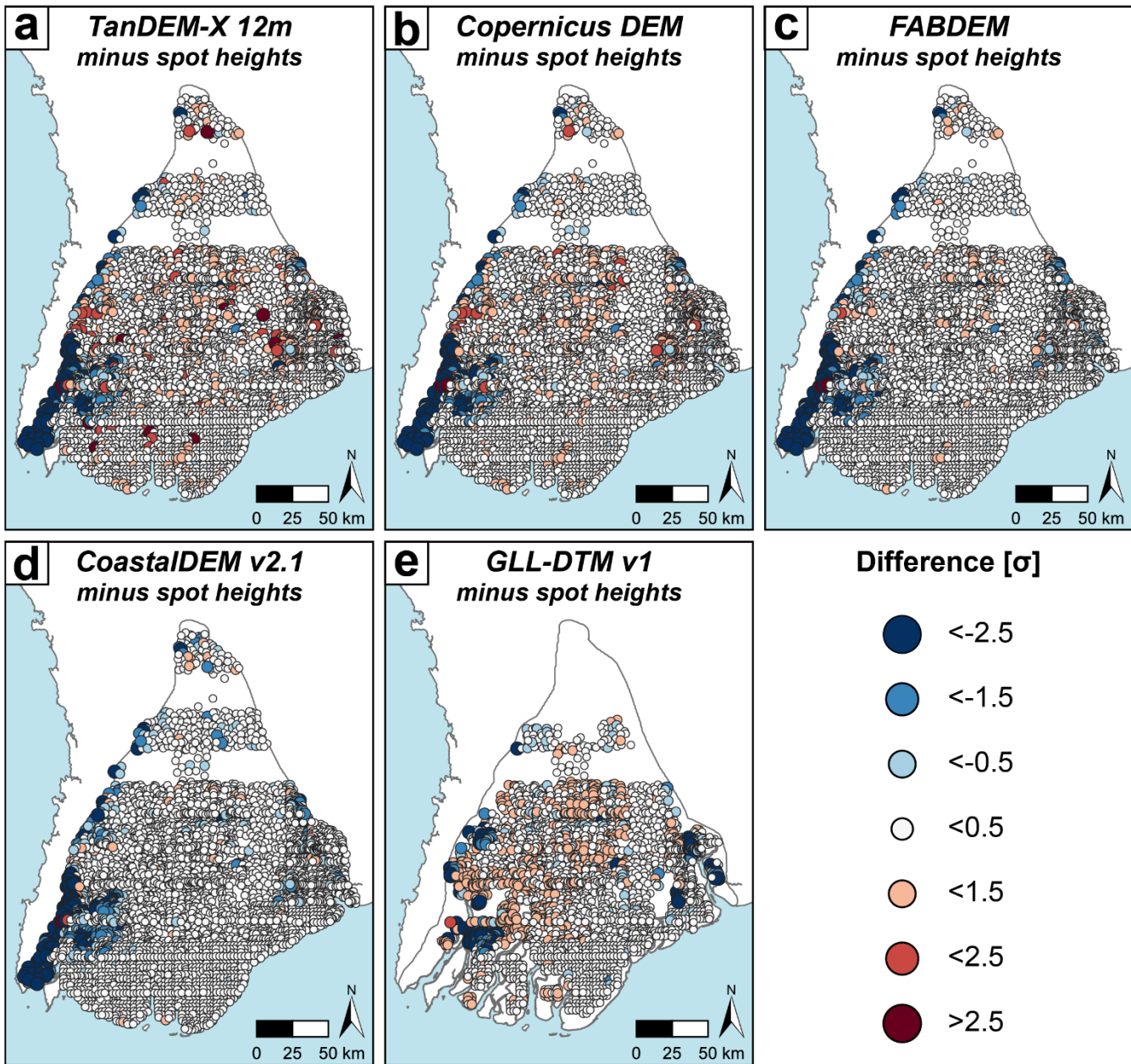
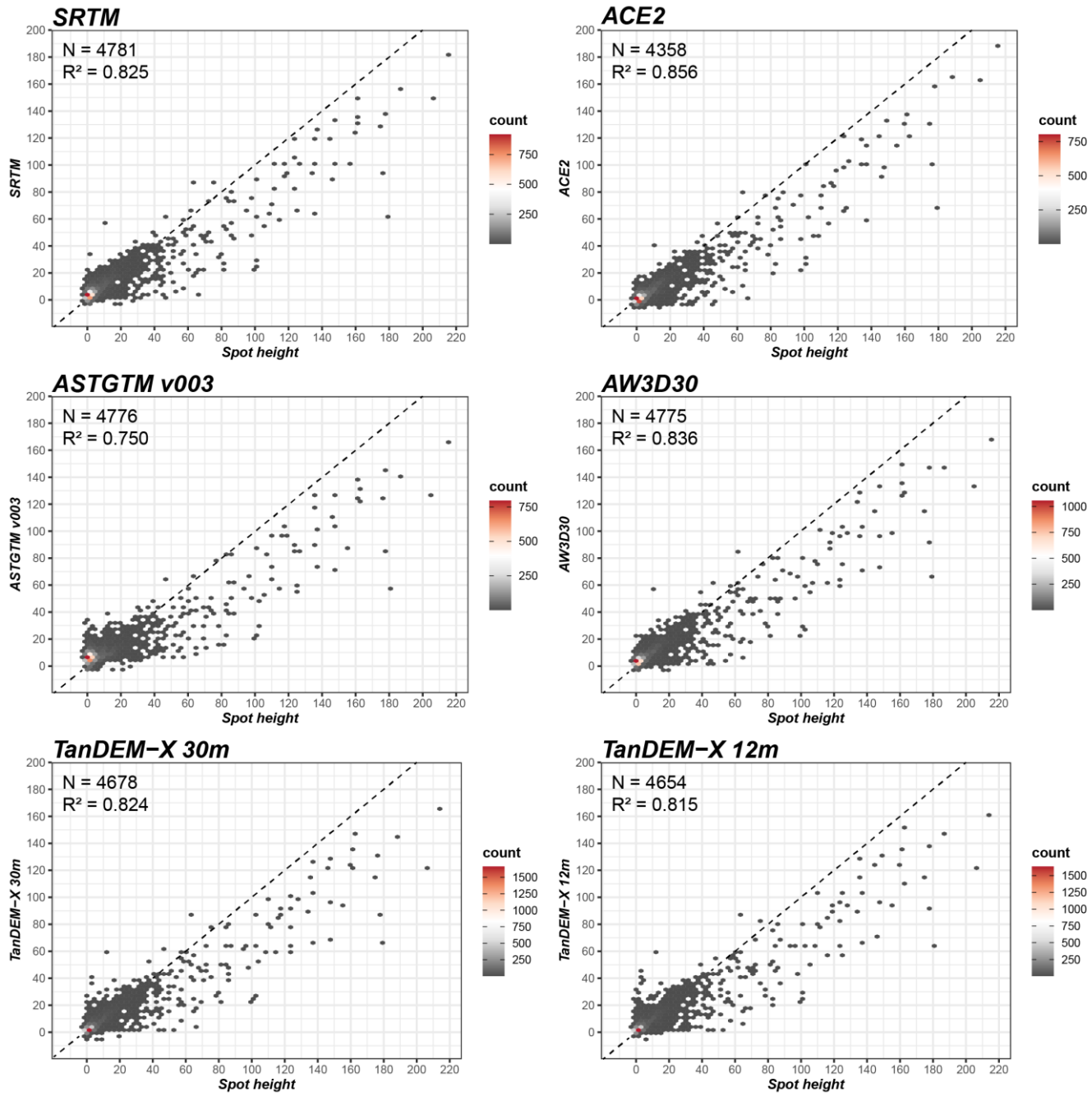


Fig. S8. Spot height residuals for global DEMs classified by standard deviation.



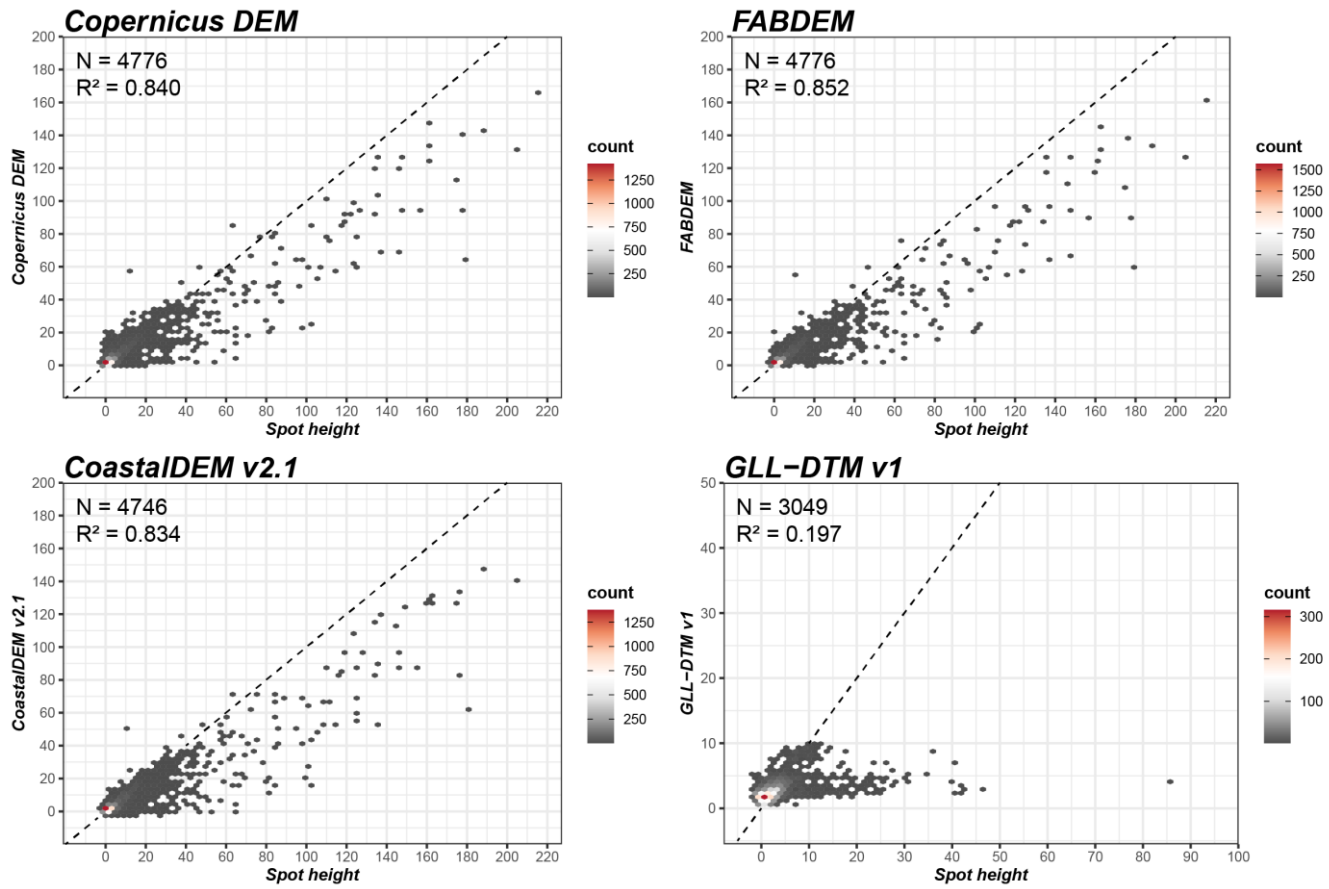


Fig. S10. 2D density plots for global DEMs in comparison with spot heights in relation to the 1:1 line.

325

Table S5. Statistics for DEMs minus spot height elevation at spot height location for the low lying delta plain (spot heights < 10 m above MSL). DEMs were used in their original resolution and vertically referenced to the same mean sea level. Note that the GLL-DTM v1 refers to a different MDT dataset than used in this study, and without being corrected for geoid offset.

| DEM | N | Mean | MAE | RMSE | Min | Max | Mean | Mean | Median | Median | Median | σ | σ | σ | R ² |
|----------|------|------|------|------|-------|-------|------|------|--------|--------|--------|------|------|------|----------------|
| | | HR | | | DEM | DEM | spot | DEM | spot | DEM | HR | spot | DEM | HR | |
| TanDEM-X | 3977 | 1.18 | 1.85 | 3.26 | -4.74 | 46.60 | 1.83 | 3.02 | 1.33 | 2.05 | 0.67 | 2.21 | 3.44 | 3.04 | 0.24 |
| 12 m | | | | | | | | | | | | | | | |
| GLL-DTM | 2893 | 0.58 | 1.38 | 1.79 | 0.36 | 9.60 | 1.78 | 2.36 | 1.35 | 2.04 | 0.62 | 2.11 | 1.37 | 1.70 | 0.35 |
| v1 | | | | | | | | | | | | | | | |

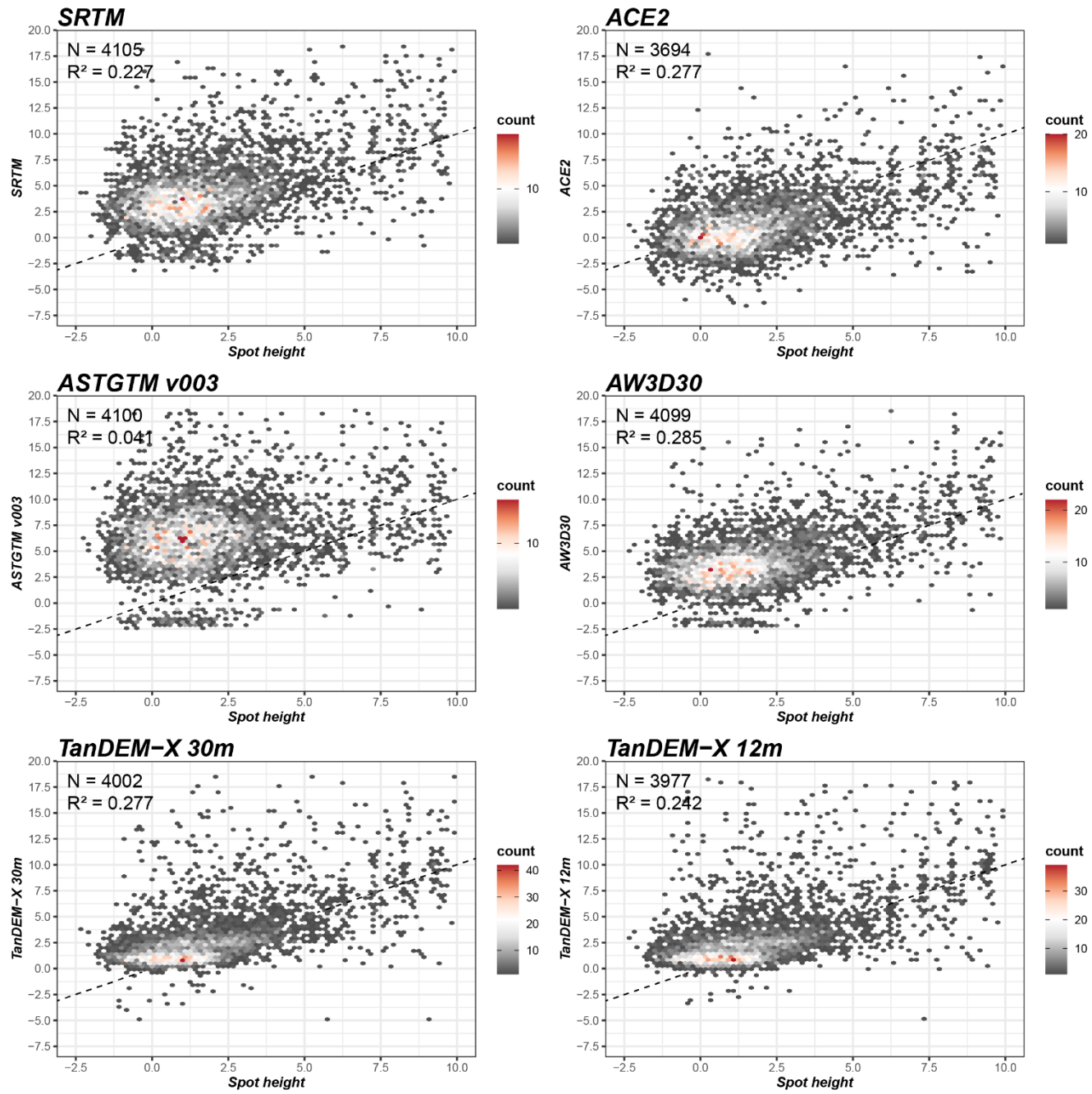
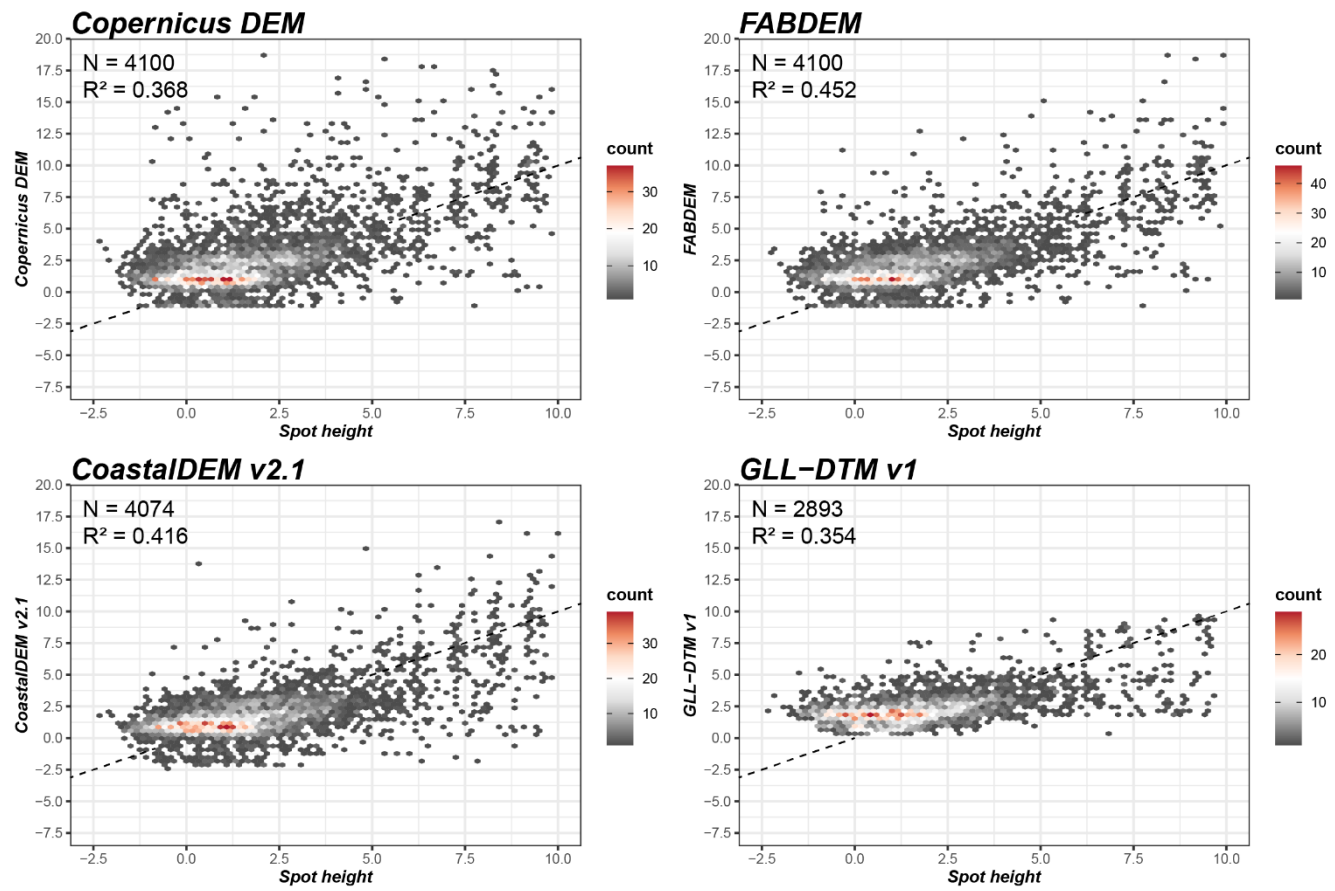


Fig. S11. 2D density plots for global DEMs in comparison with spot heights of less than 10 m above MSL in relation to the 1:1 line. For better visualisation, the maximum of the y axis was limited to 20 m and higher DEM elevations are not shown.



335 **Fig. S12.** 2D density plots for global DEMs in comparison with spot heights of less than 10 m above MSL in relation to the 1:1 line. For better visualisation, the maximum of the y axis was limited to 20 m and higher DEM elevations are not shown.

S2.2.3. Direct validation of global DEMs with AD-DEM

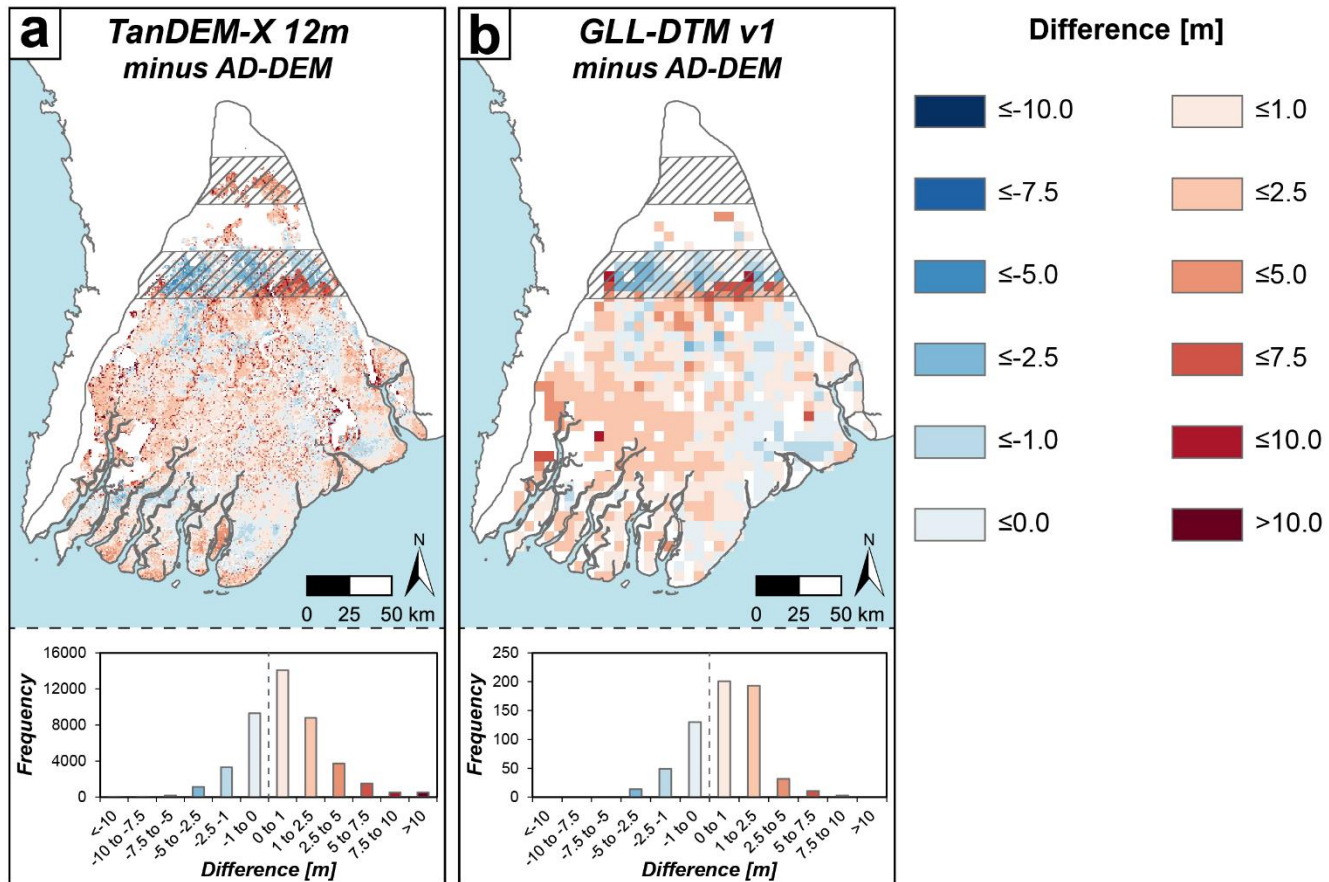


Fig. S13. Differences between global DEMs and the AD-DEM together with frequency distributions of height residuals (in m). Note that for calculating differences between GLL-DTM v1 and AD-DEM, the AD-DEM was used with a resolution of 0.05°. Areas where AD-DEM has interpolation artefacts are hashed.

Table S6. Statistics for DEM minus AD-DEM. Best performances are shown in italics. Elevations located in the centre of individual raster cells of AD-DEM were subtracted from those extracted from all other DEMs, respectively. DEMs were resampled to 750 m to match the horizontal resolution of the AD-DEM. All DEMs were referenced to mean sea level. Elevations < -7.00 m above sea level and outcrops were excluded and water masks applied.

| DEM | N | Mean | MAE | RMSE | Min | Max | Mean | Mean | Median | Median | Median | σ | σ | σ | R ² |
|------|-------|-------|-------|------|-------|-------|------|------|--------|--------|--------|----------|----------|----------|----------------|
| | | HR | | | DEM | DEM | AD- | DEM | AD- | DEM | HR | AD- | DEM | HR | |
| | | | | | | | DEM | DEM | | | | | | | DEM |
| SRTM | 40043 | 2.55 | 2.89 | 3.83 | -5.73 | 39.01 | 2.13 | 4.68 | 1.31 | 3.86 | 2.22 | 2.44 | 3.27 | 2.86 | 0.28 |
| ACE2 | 36398 | -0.47 | -1.94 | 2.68 | -6.40 | 31.86 | 2.18 | 1.71 | 1.34 | 0.94 | -0.67 | 2.50 | 3.07 | 2.64 | 0.32 |

| | | | | | | | | | | | | | | | |
|------------|-------|-------|------|------|-------|-------|------|------|------|------|------|------|------|------|------|
| ASTGTM | 39303 | 4.87 | 5.17 | 6.10 | -0.37 | 47.23 | 2.13 | 7.00 | 1.32 | 6.41 | 4.75 | 2.45 | 3.24 | 3.67 | 0.04 |
| v003 | | | | | | | | | | | | | | | |
| AW3D30 | 39313 | 2.23 | 2.62 | 3.43 | -6.97 | 51.61 | 2.16 | 4.38 | 1.30 | 3.68 | 2.07 | 2.48 | 2.99 | 2.62 | 0.31 |
| TanDEM-X | 37989 | 0.94 | 1.61 | 2.74 | -6.72 | 43.31 | 2.15 | 3.09 | 1.29 | 2.03 | 0.49 | 2.48 | 3.18 | 2.57 | 0.38 |
| 30 m | | | | | | | | | | | | | | | |
| TanDEM-X | 37961 | 0.93 | 1.58 | 2.62 | -6.16 | 29.68 | 2.15 | 3.08 | 1.29 | 2.05 | 0.51 | 2.48 | 3.09 | 2.45 | 0.40 |
| 12 m | | | | | | | | | | | | | | | |
| Copernicus | 35854 | 0.91 | 1.55 | 2.57 | -1.15 | 32.46 | 2.17 | 3.08 | 1.29 | 2.05 | 0.50 | 2.50 | 3.05 | 2.40 | 0.41 |
| DEM | | | | | | | | | | | | | | | |
| FABDEM | 35843 | 0.63 | 1.27 | 2.00 | -0.85 | 31.18 | 2.17 | 2.80 | 1.29 | 1.89 | 0.46 | 2.50 | 2.61 | 1.90 | 0.53 |
| CoastalDEM | 40015 | 0.17 | 1.17 | 1.75 | -4.71 | 27.61 | 2.12 | 2.29 | 1.31 | 1.41 | 0.19 | 2.44 | 2.38 | 1.74 | 0.55 |
| v2.1 | | | | | | | | | | | | | | | |
| GLL-DTM | 30724 | 0.674 | 1.15 | 1.57 | 0.32 | 9.71 | 1.98 | 2.66 | 1.30 | 2.13 | 0.66 | 2.24 | 1.70 | 1.41 | 0.60 |
| v1 | | | | | | | | | | | | | | | |

S2.2.4. Recent flood events in the Ayeyarwady Delta and indirect validation of DEMs with flood mappings/flood-prone areas

350 Recent precipitation and flood events in the Ayeyarwady Delta: The Indian monsoon seasons 2015 and 2020

Aside the long-term risk of SLR and coastal storm surges due to tropical cyclones that make landfall in the region (e.g., Brakenridge et al., 2017; Brill et al., 2020), climatological hazards in Myanmar and the Ayeyarwady Delta are heat waves, droughts, as well as extreme precipitation, subsequent floods, and landslides, all of them related to the spatiotemporal variability of the monsoon regime (e.g., Horton et al., 2017; Masson-Delmotte et al., 2021; Zin Mie Mie Sein et al., 2022 and references therein). Flood events in the delta after cyclone Nargis 2008 were mainly induced by heavy rains and increased

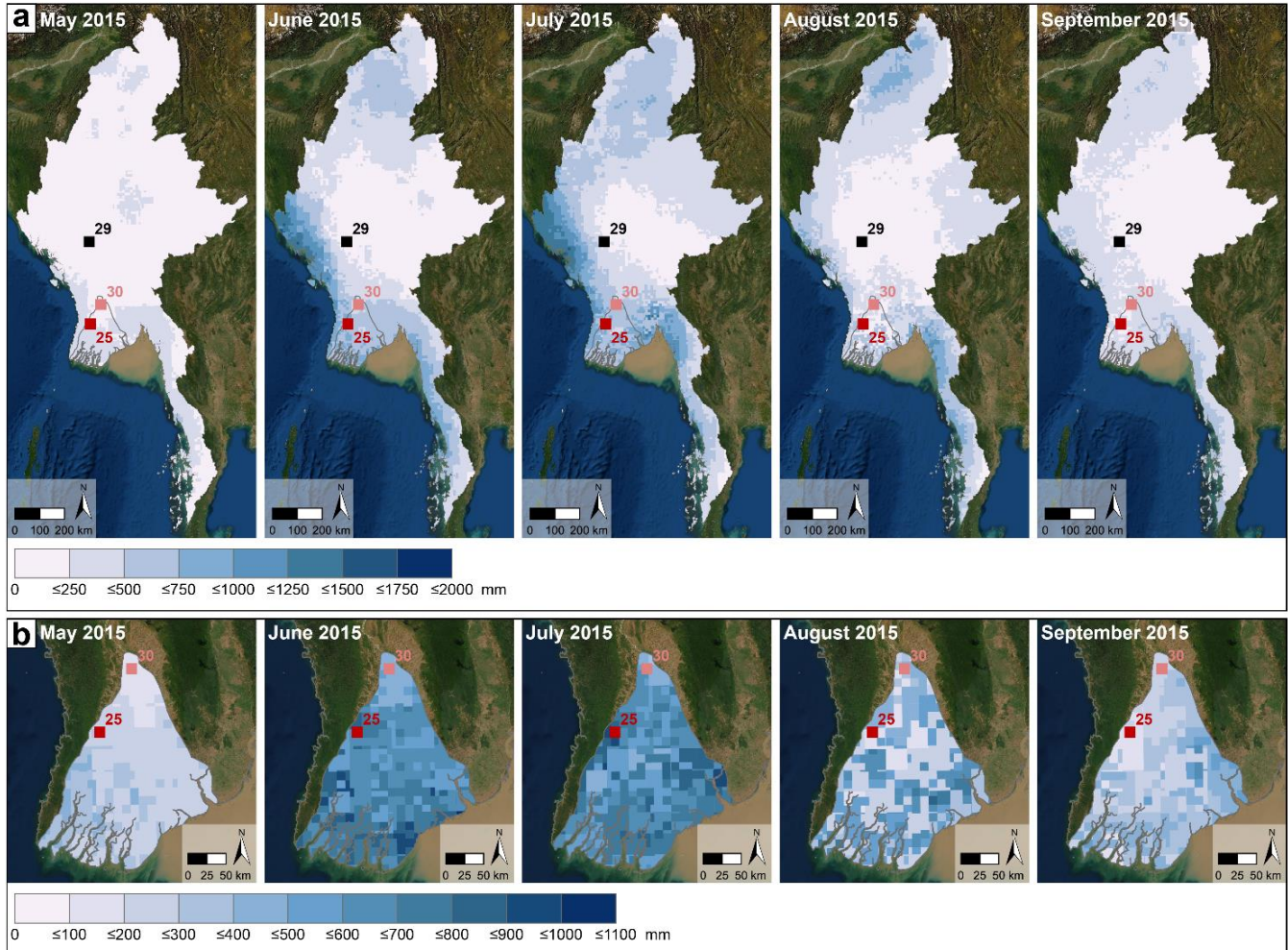
355 discharges during the Indian Monsoon season (e.g., Brakenridge et al., 2017; Myanmar Information Management Unit (MIMU), 2017, 2020; UN Office for the Coordination of Humanitarian Affairs (OCHA), 2017, 2018, 2020). In 2015, country-wide flooding occurred due to exceptionally intense monsoon precipitation, which can be related to phases 5 and 6 of a strong Madden–Julian Oscillation (Brakenridge et al., 2017; Da Silva and Matthews, 2021), and that was accompanied by additional

360 rainfalls of tropical cyclone Komen that made landfall in Bangladesh (Government of the Union of Myanmar, 2015). Precipitation amounts exceeded average monsoonal rainfalls by up to 400 % (Brakenridge et al., 2017), and resulted in flooding of unprecedented extent, affecting more than 1.6 million people (with 132 deaths), and up to 530,000 ha of agricultural and aquacultural production areas (Brakenridge et al., 2017; IFRC, 2017; Government of the Union of Myanmar, 2015).

Within the defined delta ROI, rainfalls occurred throughout the monsoonal period, especially from June to August.

365 Precipitation peaked at maximum 987 mm accumulated in July, whereas the maximum countrywide was more than 1,800 mm (Fig. S14). River discharge behaves slightly time-elapsed to precipitation, showing maximum discharges in July, August,

September, and October (Fig. S15). Thereby, the discharge amounts nicely reflect how the distributaries buffer upstream runoff. Flooding occurred already by mid of August (Copernicus Emergency Management Service, 2015), but was most extensive in deltaic districts in September (i.e., Pathein, Hinthada, Bago West and Ma-ubin) with more than 3250 km² of the 370 ROI being flooded (Figs. 5 and S19).



375 **Fig. S14.** Monthly accumulated precipitation in Myanmar (a) and the Ayeyarwady Delta (b) for the monsoon season 2015 together with locations of microwave discharge measurement sites (Brakenridge et al., 2022) based on Esri World Imagery (2017).

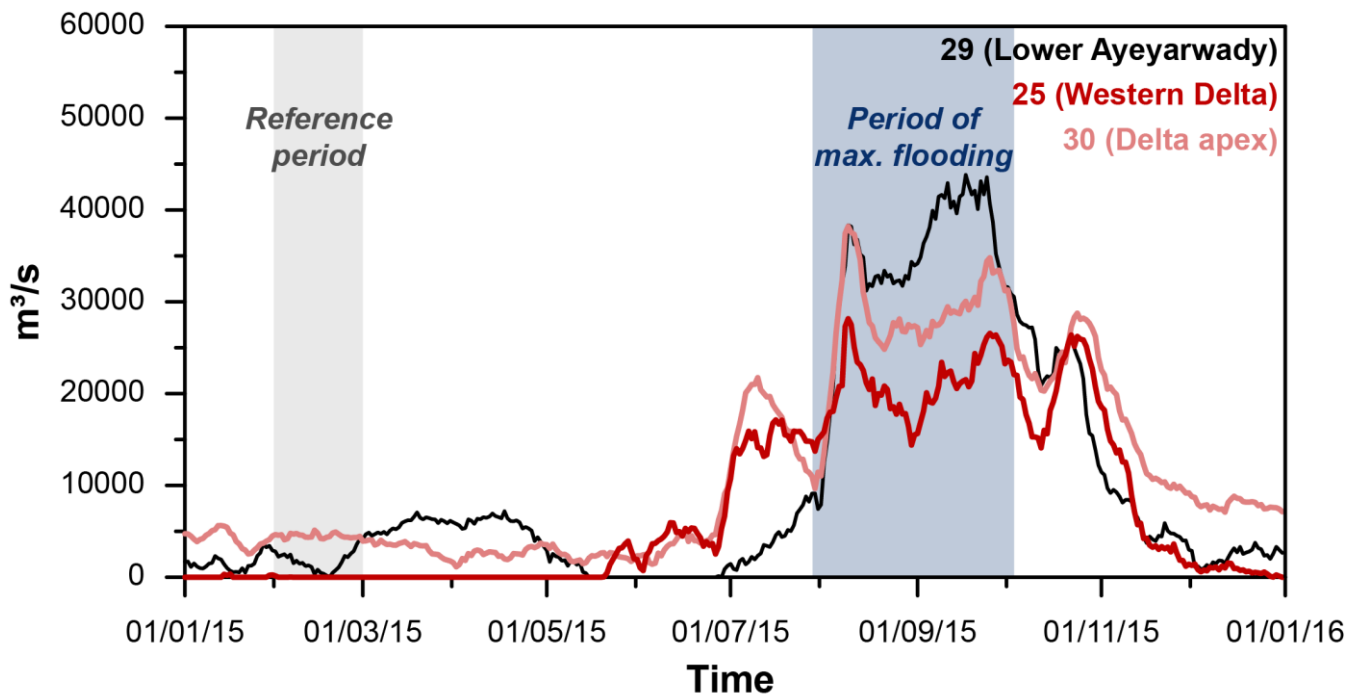


Fig. S15. Discharge pattern of the monsoon season 2015. 10 day average discharges are shown for River Watch stations 25, 29, and 30 located at the Ayeyarwady River. Data were accessed via the River and Reservoir Watch Version 4.5 processor of the Dartmouth Flood Observatory (Brakenridge et al., 2022).
380

In contrast, the 2020 monsoon season was moderate (Department of Meteorology and Hydrology (DMH), 2020). Monsoonal precipitation was accompanied by additional rainfalls of tropical storm Noul that made landfall in Vietnam (ECHO, 2020). 4 deaths were reported due to a landslide event in Mandalay Region (OCHA, 2020), and at least 21,500 people were affected by 385 overflow of the Ayeyarwady and Thanlyin Rivers (Mi Mi Tun, 2020). However, since ca. 1,950 km² were inundated in the Ayeyarwady and Bago (West) Regions by 1st September, probably up to 267,277 people were exposed to flooded areas (MIMU, 2020).

From the GPM data, we reveal maximum rainfall in Myanmar of more than 1600 mm accumulated in Myingun Island south of Sittwe in August, whereas in the delta, monthly accumulated precipitation peaked at 833 mm (Fig. S16). Generally, the 390 2020 rainfalls reflect stronger intra-seasonal variability than 2015, which is also reflected by the discharge period. While flooding occurred from June to September, it was most extensive by the end of August, following maximum discharge and amounting to more than 2,700 km² (Figs. 5, S17 and S19). In line with the 2020 precipitation pattern, where highest rainfall amounts were accumulated in the most seaward delta parts as compared to 2015, also the flooded areas of 2020 extend further south than in 2015 (Figs. 5 and S19). It is therefore likely that these delineated areas not only become flooded due to river and 395 channel overflow but also because of water saturation of the soils.

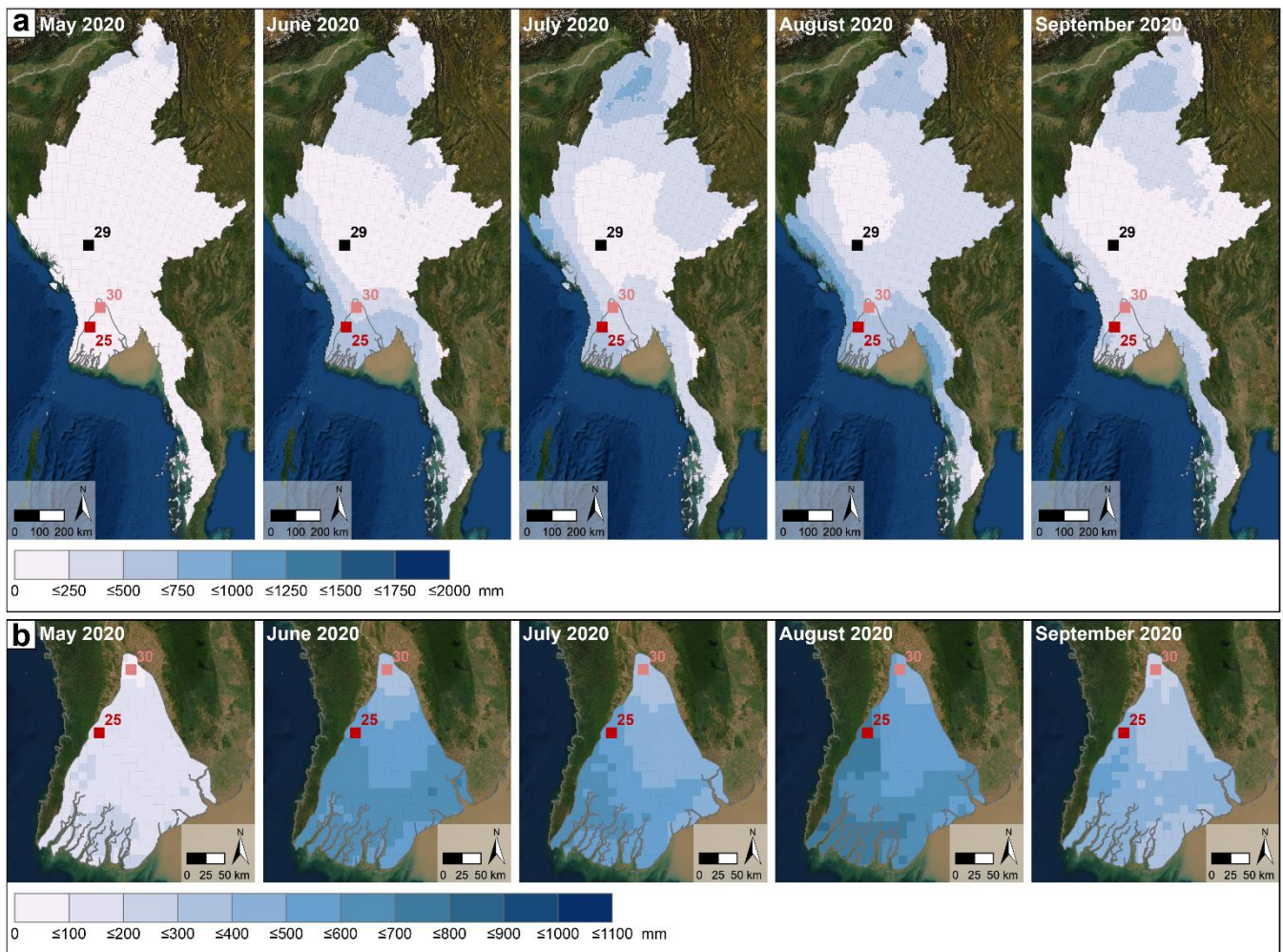


Fig. S16. Monthly accumulated precipitation in Myanmar (a) and the Ayeyarwady Delta (b) for the monsoon season 2020 together with locations of microwave discharge measurement sites (Brakenridge et al., 2022) based on Esri World Imagery

400 (2017).

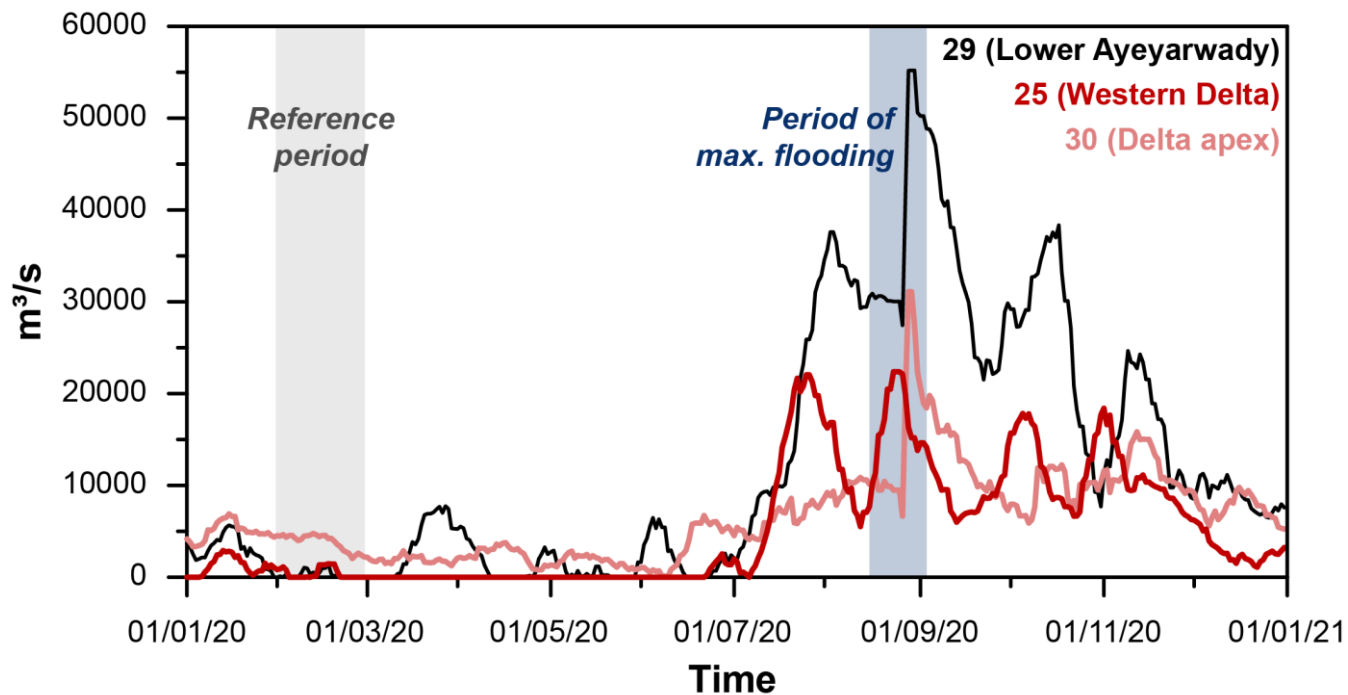
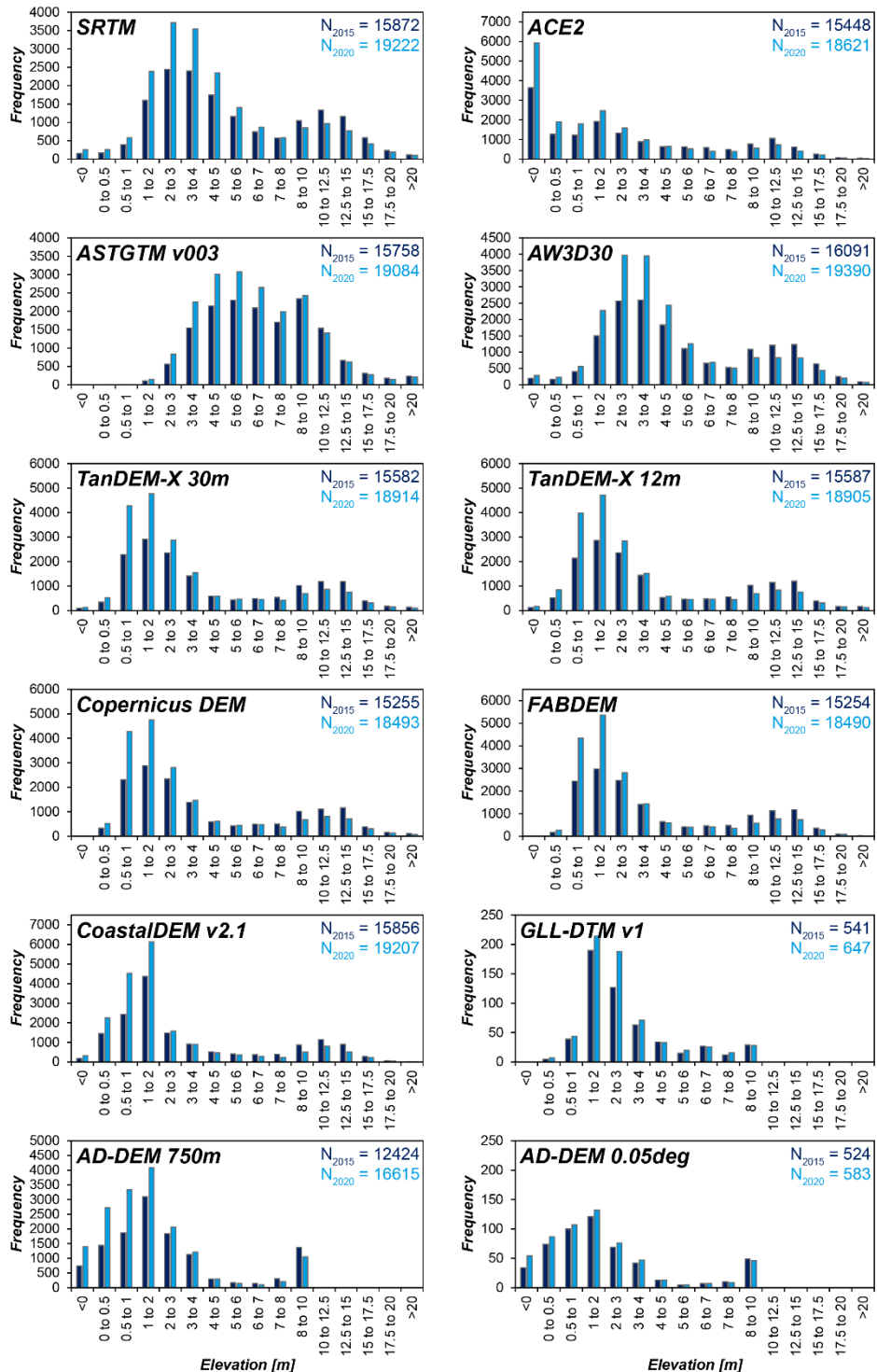


Fig. S17. Discharge pattern of the monsoon season 2020. 10 day average discharges are shown for River Watch stations 25, 29, and 30 located at the Ayeyarwady River. Data were accessed via the River and Reservoir Watch Version 4.5 processor of

405

the Dartmouth Flood Observatory (Brakenridge et al., 2022).



410 **Fig. S18.** Frequency distribution of elevation counts (in m) for DEMs inside areas affected by flooding during the monsoon season of 2015 (dark blue) and 2020 (light blue).

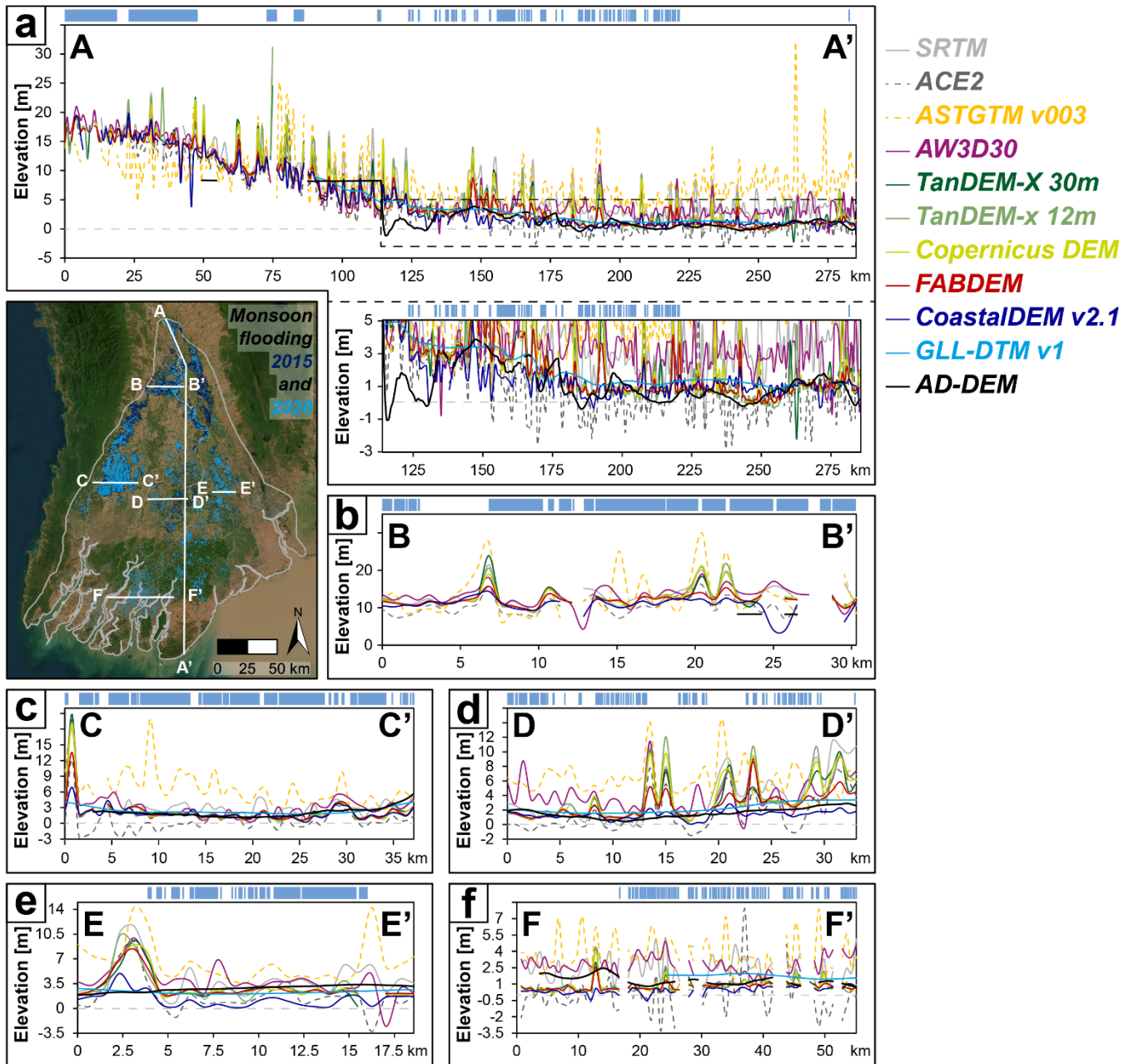
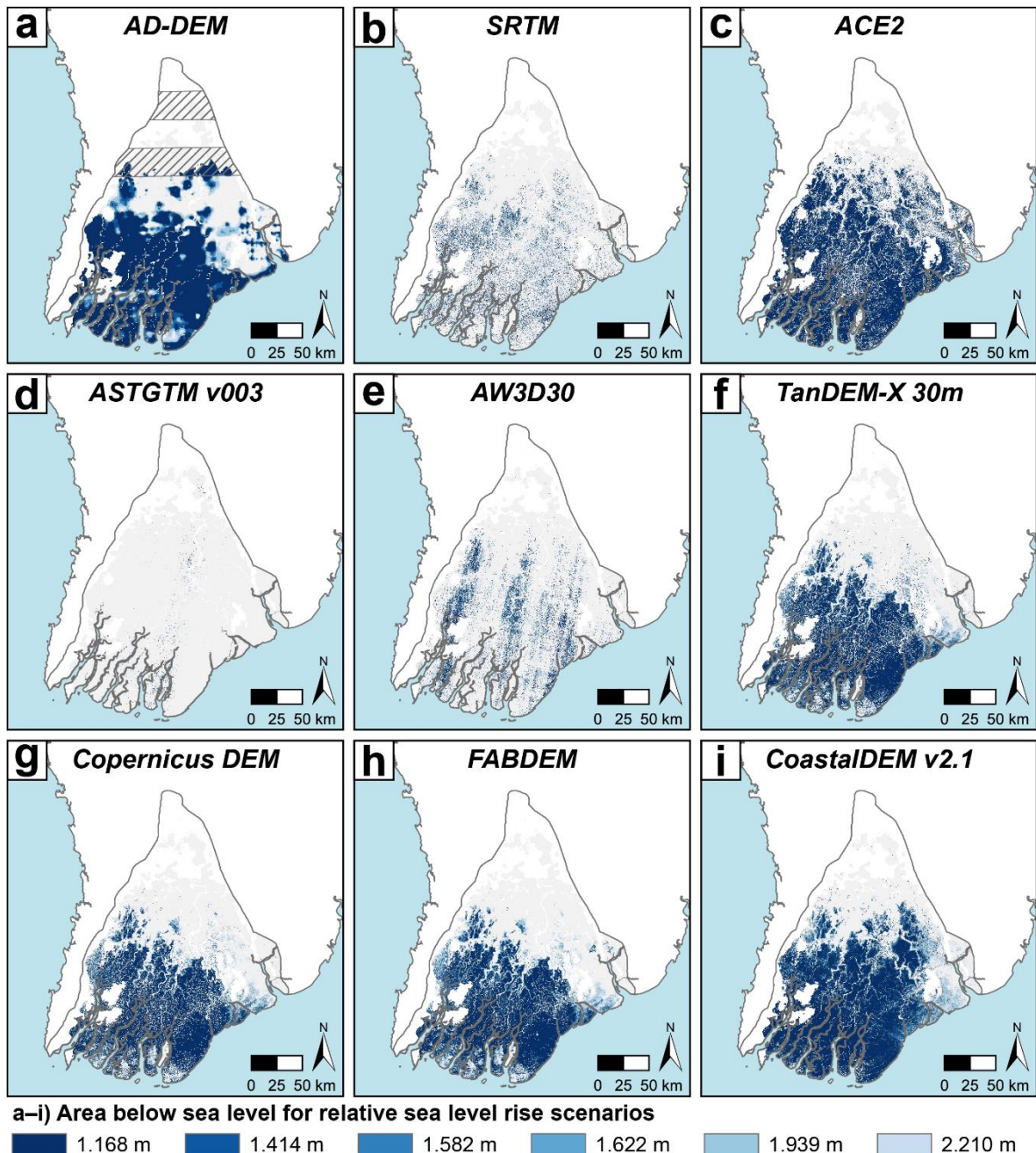
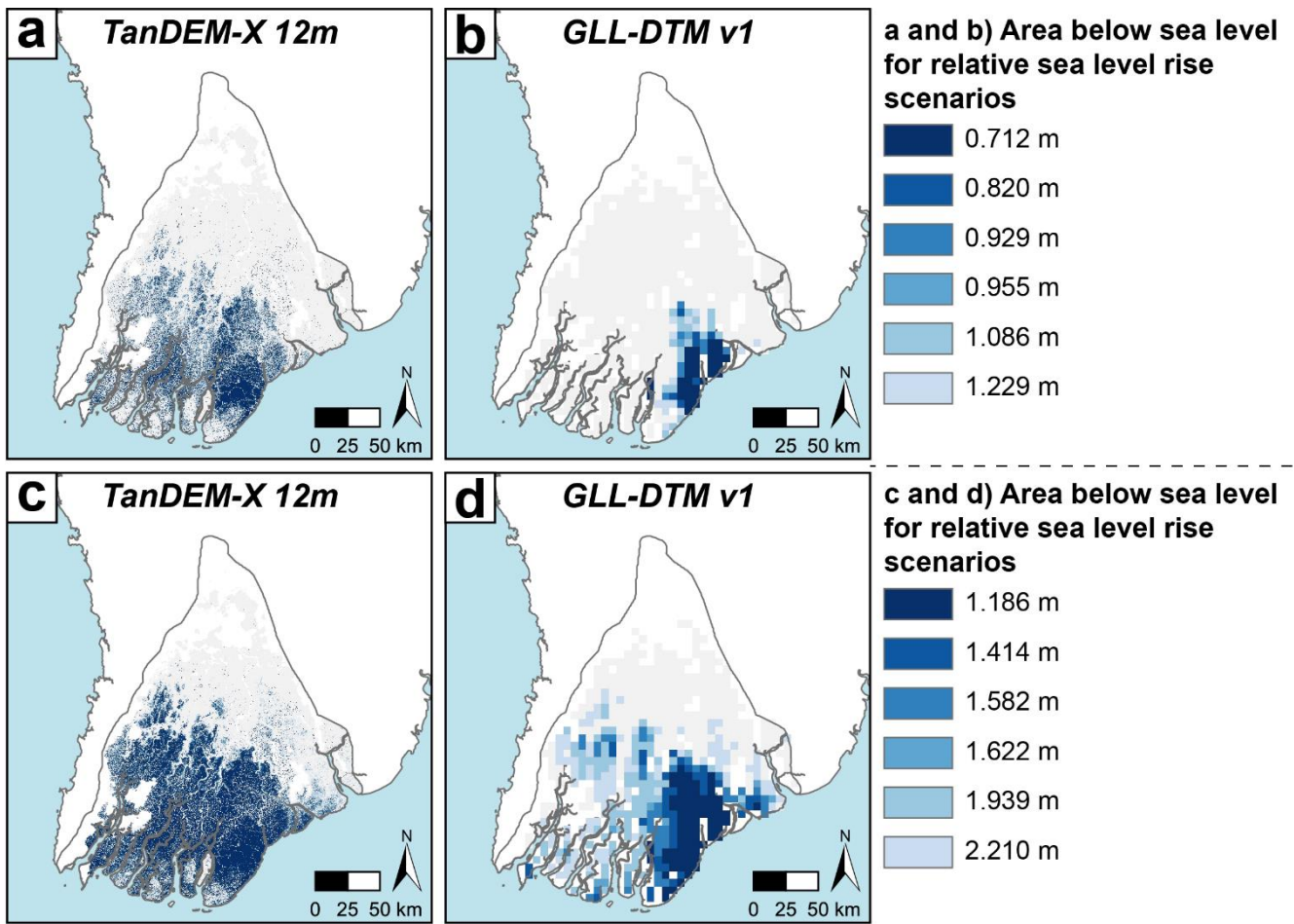


Fig. S19. Delta elevation along longitudinal (a) and cross sections (b–f) in deltaic areas affected by flooding during the monsoon seasons 2015 and 2020 (Base map: Esri World Imagery, 2017). Elevation profiles are based on DEMs resampled to 415 750 m spatial resolution, except of the GLL-DTM v1, which was used in its original resolution of 0.05°. Blue bars on top of the profiles indicate the location of inundated areas along the profiles. The black-dashed rectangle in (a) marks the low elevation zone along the longitudinal profile that is also shown enlarged.

S2.3. Estimation of low lying coastal area at risk of future sea level rise



420 **Fig. S20.** Area below future mean sea level according to local and global DEMs following median sea level rise projections for Yangon for 2150 (compared to the baseline period 1995–2014) from the Sea Level Projection Tool of the IPCC 6th Assessment Report (Fox-Kemper et al., 2021; Garner et al., 2021; 2022). Note that in case of higher RSLR, these scenarios will be reached sooner than 2150.



425 **Fig. S21.** Area below future mean sea level according to global DEMs, which were excluded from the main text, following median sea level rise projections for Yangon for 2100 (a and b) and 2150 (c and d) (compared to the baseline period 1995–2014) from the Sea Level Projection Tool of the IPCC 6th Assessment Report (Fox-Kemper et al., 2021; Garner et al., 2021; 2022). Note that in case of higher RSLR, these scenarios will be reached sooner than 2100 and 2150, respectively.

430 **Table S7.** Area and population below sea level for selected relative sea level rise scenarios taken from projections of the IPCC 6th Assessment Report for the years of 2100 and 2150, respectively. Estimates of the 50th percentile from the intermediate SSP2-4.5 reference scenario and 83rd percentile from the high SSP5-8.5 reference scenario are given as they constitute lower and upper boundaries of pathway probability. Note that the category of 0 m sea level rise includes areas that are already below sea level.

435 DEMs were used in their original resolution, with water and outcrop masks applied and erroneous elevation data (< -7.00 m) excluded. Area and population estimates are based on administrative districts in the delta ROI that have been masked for outcrops. Note that the outline of administrative units slightly differs from the ROI along the coast and some river channels,

likely related to different dates of data generation and underlying source data, together with the impact of coastal and fluvial dynamics (see also Fig. S28).

Present

| 0 m SLR | | | | |
|-----------------|----------------------------|--------------|---------------------------------------------------------|------------------------------------|
| | Area in km ² | Area in % | Population (as of 2020) as a number (×100,000) | Population (as of 2020) in % |
| SRTM | 501.00 | 1.92 | 1.26 | 0.83 |
| ACE2 | 7586.13 | 29.12 | 19.59 | 12.90 |
| ASTGTM | 4.55 | 0.02 | 0.01 | 0.01 |
| v003 | | | | |
| AW3D30 | 439.65 | 1.69 | 1.20 | 0.79 |
| TanDEM-X | 251.01 | 0.96 | 0.73 | 0.48 |
| 30 m | | | | |
| Copernicus DEM | 115.04 | 0.44 | 0.24 | 0.16 |
| FABDEM | 60.83 | 0.23 | 0.13 | 0.08 |
| CoastalDEM v2.1 | 449.97 | 1.73 | 0.95 | 0.63 |
| GLL-DTM v1 | 0.00 | 0.00 | 0.00 | 0.00 |
| AD-DEM | 2268.15 | 8.71 | 6.75 | 4.45 |

As projected for 2100 (but may be reached sooner)

| | 0.712 m SLR (SSP2-4.5 50th Percentile) | | | | 1.229 m SLR (SSP5-8.5 83rd Percentile) | | | |
|----------|----------------------------------------------------------|--------------|---------------------------------------------------------|----------------------------|----------------------------------------------------------|--------------|---------------------------------------------------------|----------------------------|
| | Area in km ² | Area in % | Population (as of 2020) as a number (×100,000) | Population (as of 2020) | Area in km ² | Area in % | Population (as of 2020) as a number (×100,000) | Population (as of 2020) |
| | | | | | | | | |
| SRTM | 1156.78 | 4.44 | 2.98 | 1.97 | 2030.60 | 7.79 | 5.06 | 3.33 |
| ACE2 | 11071.96 | 42.49 | 30.02 | 19.78 | 13359.58 | 51.27 | 38.03 | 25.05 |
| ASTGTM | 18.54 | 0.07 | 0.04 | 0.03 | 32.44 | 0.13 | 0.062 | 0.04 |
| v003 | | | | | | | | |
| AW3D30 | 1004.13 | 3.85 | 2.64 | 1.74 | 1829.36 | 7.02 | 4.67 | 3.07 |
| TanDEM-X | 2559.90 | 9.83 | 5.45 | 3.59 | 8233.78 | 31.60 | 17.91 | 11.80 |
| 30 m | | | | | | | | |

| | | | | | | | | |
|-----------------|---------|-------|-------|-------|----------|-------|-------|-------|
| Copernicus DEM | 2402.78 | 9.22 | 4.87 | 3.21 | 8059.50 | 30.93 | 17.24 | 11.35 |
| FABDEM | 1814.61 | 6.96 | 3.59 | 2.37 | 7989.57 | 30.66 | 17.25 | 11.37 |
| CoastalDEM v2.1 | 4561.33 | 17.51 | 9.60 | 6.33 | 11049.32 | 42.41 | 24.74 | 16.30 |
| GLL-DTM v1 | 1088.12 | 4.18 | 2.24 | 1.47 | 2832.93 | 10.87 | 5.94 | 3.91 |
| AD-DEM | 8152.00 | 31.29 | 20.14 | 13.27 | 12160.47 | 46.67 | 29.35 | 19.33 |

As projected for 2150 (but may be reached sooner)

| 1.168 m SLR (SSP2-4.5 50 th Percentile) | | | | 2.210 m SLR (SSP5-8.5 83 rd Percentile) | | | | |
|----------------------------------------------------|-------------------------|-----------|------------------------------------------------|----------------------------------------------------|-------------------------|-----------|------------------------------------------------|-------|
| | Area in km ² | Area in % | Population (as of 2020) as a number (×100,000) | Population (as of 2020) in % | Area in km ² | Area in % | Population (as of 2020) as a number (×100,000) | |
| SRTM | 1923.39 | 7.38 | 4.79 | 3.12 | 5085.83 | 19.52 | 12.93 | 8.52 |
| ACE2 | 13108.30 | 50.31 | 37.18 | 24.49 | 16369.05 | 62.82 | 51.81 | 34.13 |
| ASTGTM v003 | 27.10 | 0.10 | 0.05 | 0.03 | 330.24 | 1.27 | 0.65 | 0.43 |
| AW3D30 | 1717.65 | 6.59 | 4.39 | 2.89 | 4890.86 | 18.77 | 12.34 | 8.13 |
| TanDEM-X 30 m | 7697.12 | 29.54 | 16.67 | 10.99 | 13304.21 | 51.06 | 31.39 | 20.68 |
| Copernicus DEM | 7525.81 | 28.88 | 16.02 | 10.55 | 13069.53 | 50.16 | 30.52 | 20.11 |
| FABDEM | 7316.11 | 28.08 | 15.64 | 10.30 | 13866.88 | 53.22 | 36.42 | 23.99 |
| CoastalDEM v2.1 | 10330.23 | 39.65 | 22.94 | 15.11 | 17597.88 | 67.54 | 50.00 | 32.94 |
| GLL-DTM v1 | 2626.11 | 10.08 | 5.51 | 3.63 | 11926.35 | 45.77 | 28.45 | 18.74 |
| AD-DEM | 11720.23 | 44.98 | 28.28 | 18.63 | 16931.31 | 64.98 | 45.95 | 30.27 |

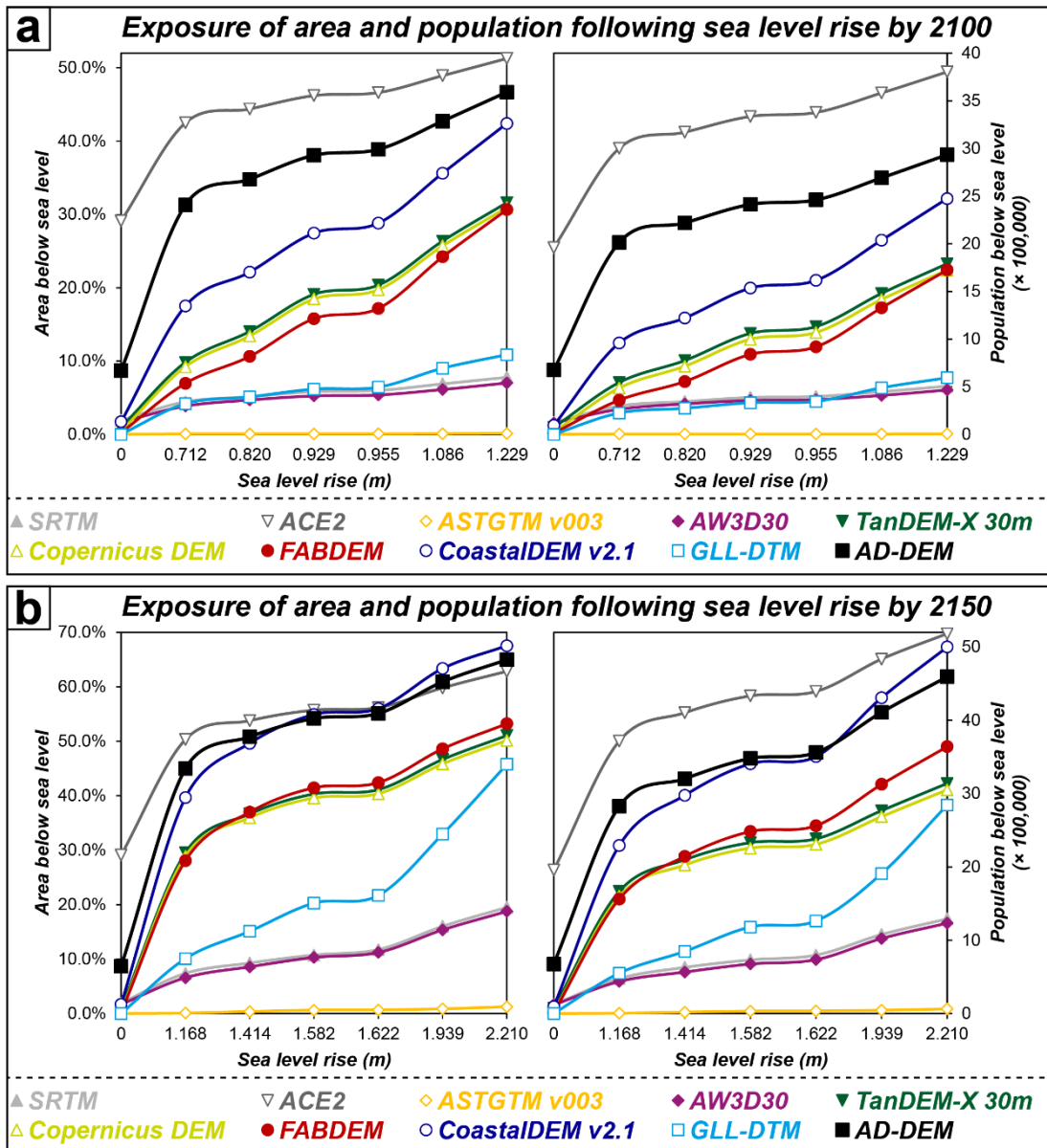
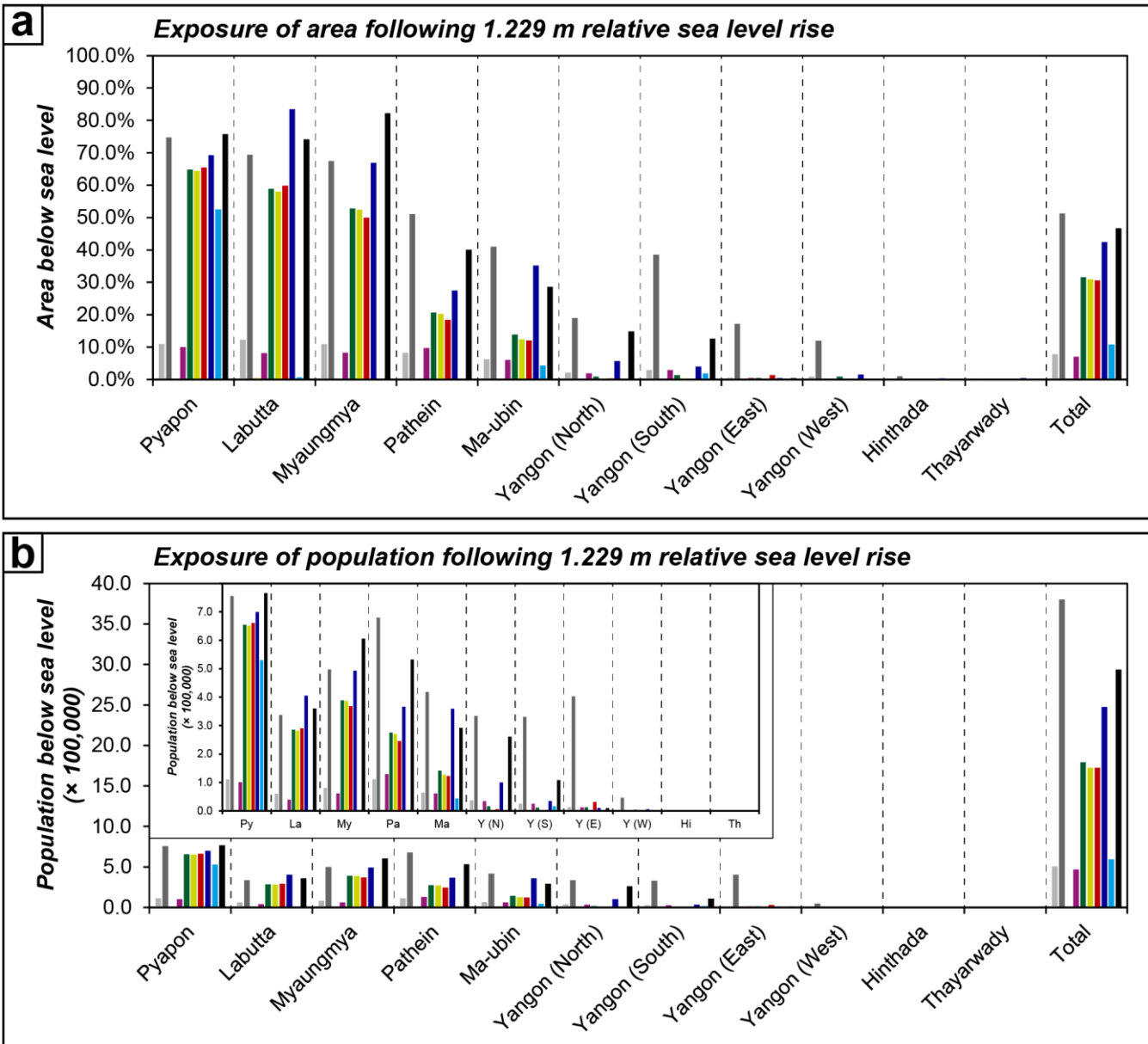
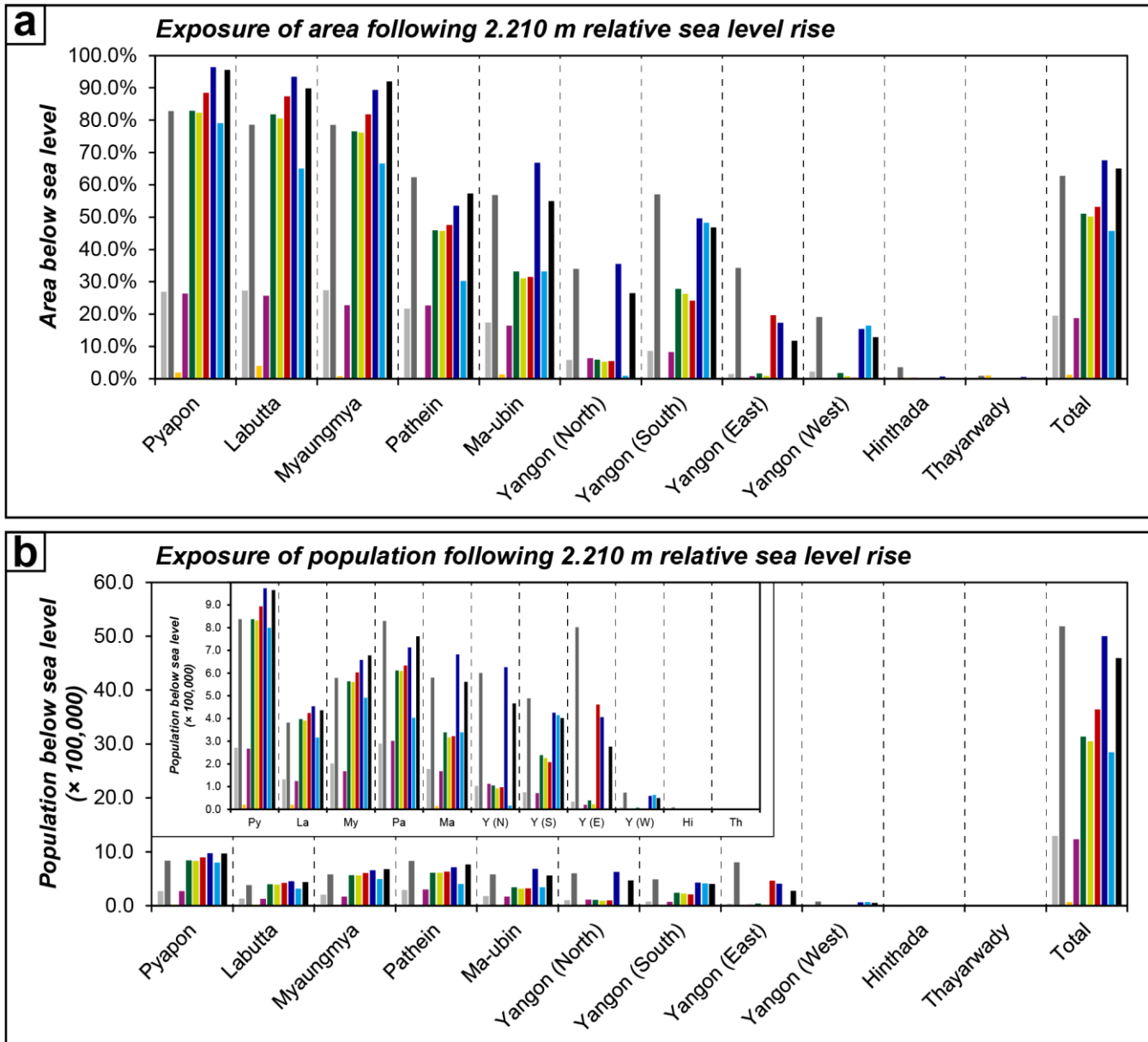


Fig. S22. Area and people that will fall below future sea level by 2100 (a) and 2150 (b) following median sea level rise projections for Yangon (compared to the baseline period 1995–2014) from the Sea Level Projection Tool of the IPCC 6th Assessment Report (Fox-Kemper et al., 2021; Garner et al., 2021; 2022). Estimates on affected people are based on LandScan Global 2020 data (Rose et al., 2021).



SRTM
Copernicus DEM **ACE2**
FABDEM **ASTGTM v003**
CoastalDEM v2.1 **AW3D30**
GLL-DTM **TanDEM-X 30m**
AD-DEM

Fig. S23. Area (a) and people (b) affected by sea level rise of 1.229 m as projected by SSP5-8.5 (83rd percentile) for 2100 for each administrative district of the Ayeyarwady Delta and the entire delta. Estimates of affected district population are enlarged in the insets. All population estimates are based on the actual population of 2020 (Rose et al., 2021).



SRTM
Copernicus DEM

ACE2
FABDEM

ASTGTM v003
CoastalDEM v2.1

AW3D30
GLL-DTM

TanDEM-X 30m
AD-DEM

Fig. S24. Area (a) and people (b) affected by sea level rise of 2.210 m as projected by SSP5-8.5 (83rd percentile) for 2150 for each administrative district of the Ayeyarwady Delta and the entire delta. Estimates of affected district population are enlarged in the insets. All population estimates are based on the actual population of 2020 (Rose et al., 2021).

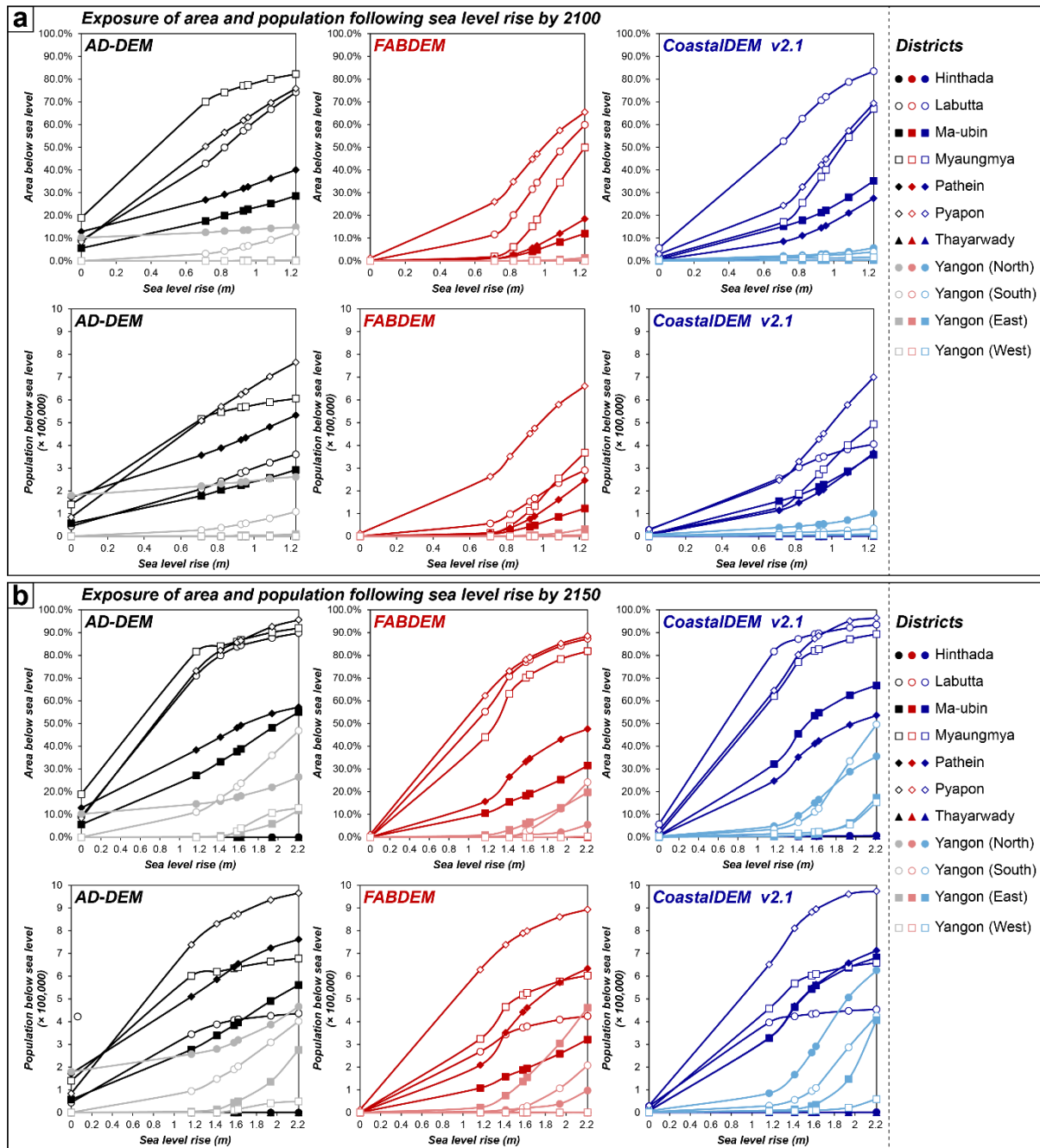


Fig. S25. Estimated percentage of administrative district area and inhabitants affected by sea level rise according to projections of the IPCC 6th Assessment Report for the years 2100 (a) and 2150 (b) based on AD-DEM, FABDEM, and CoastalDEM v2.1, respectively. DEMs were used in their original resolution, with water and outcrop masks applied and erroneous elevation data (< -7.00 m) excluded. Area and population estimates are based on administrative districts in the delta ROI that have been masked for outcrops. All population estimates are based on the actual population of 2020 (Rose et al., 2021).

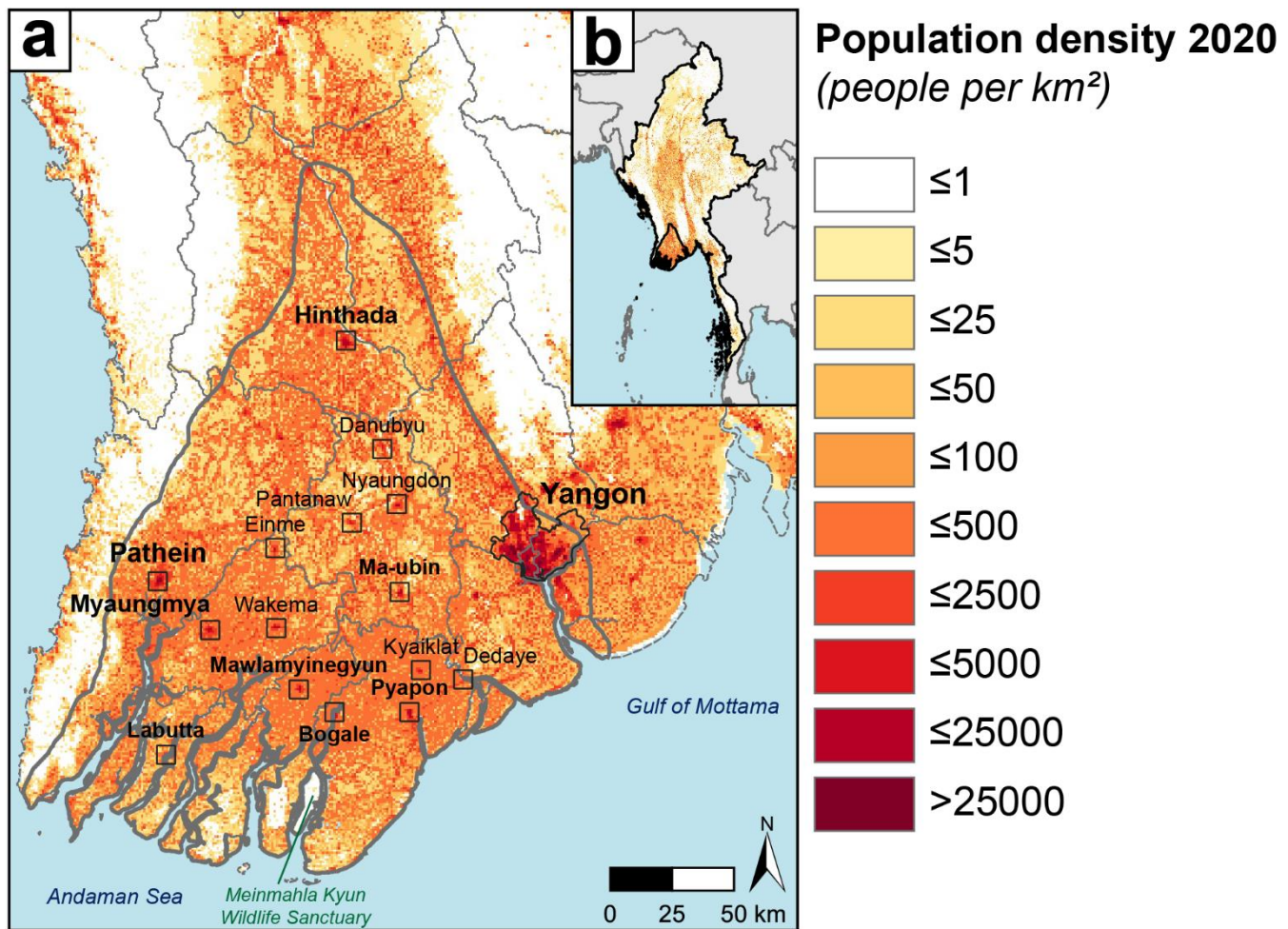


Fig. S26. Population density in the Ayeyarwady Delta (a) and in Myanmar (b; based on LandScan Global 2020 population data (Rose et al., 2021)) together with the location of major cities and urban settlements that will be most affected by future sea level rise. The location of the Meinmahla Kyun Wildlife Sanctuary is shown as well.

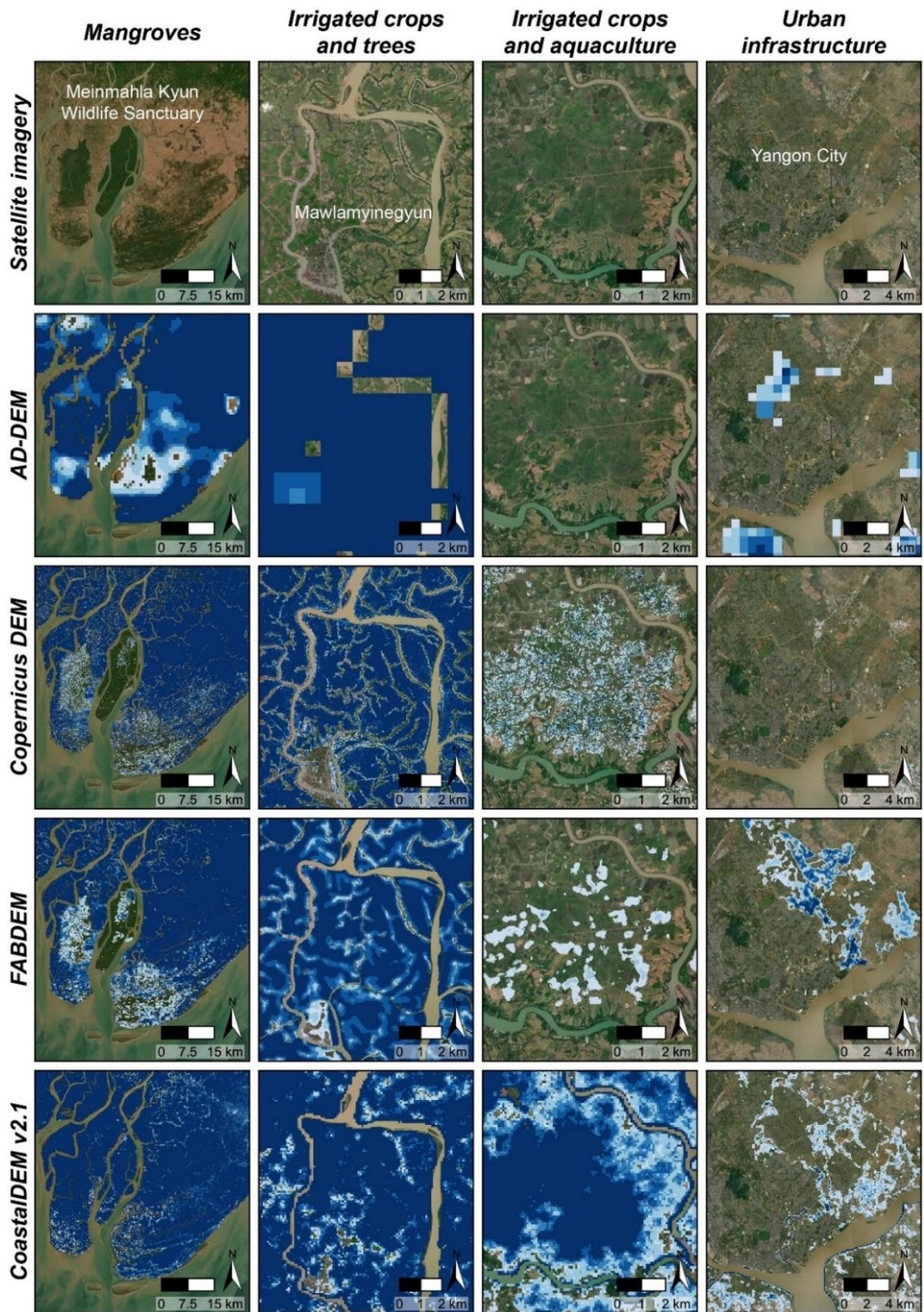


Fig. S27. Performance of selected DEMs in sea level rise impact assessments for 2150 in relation to land cover based on Esri

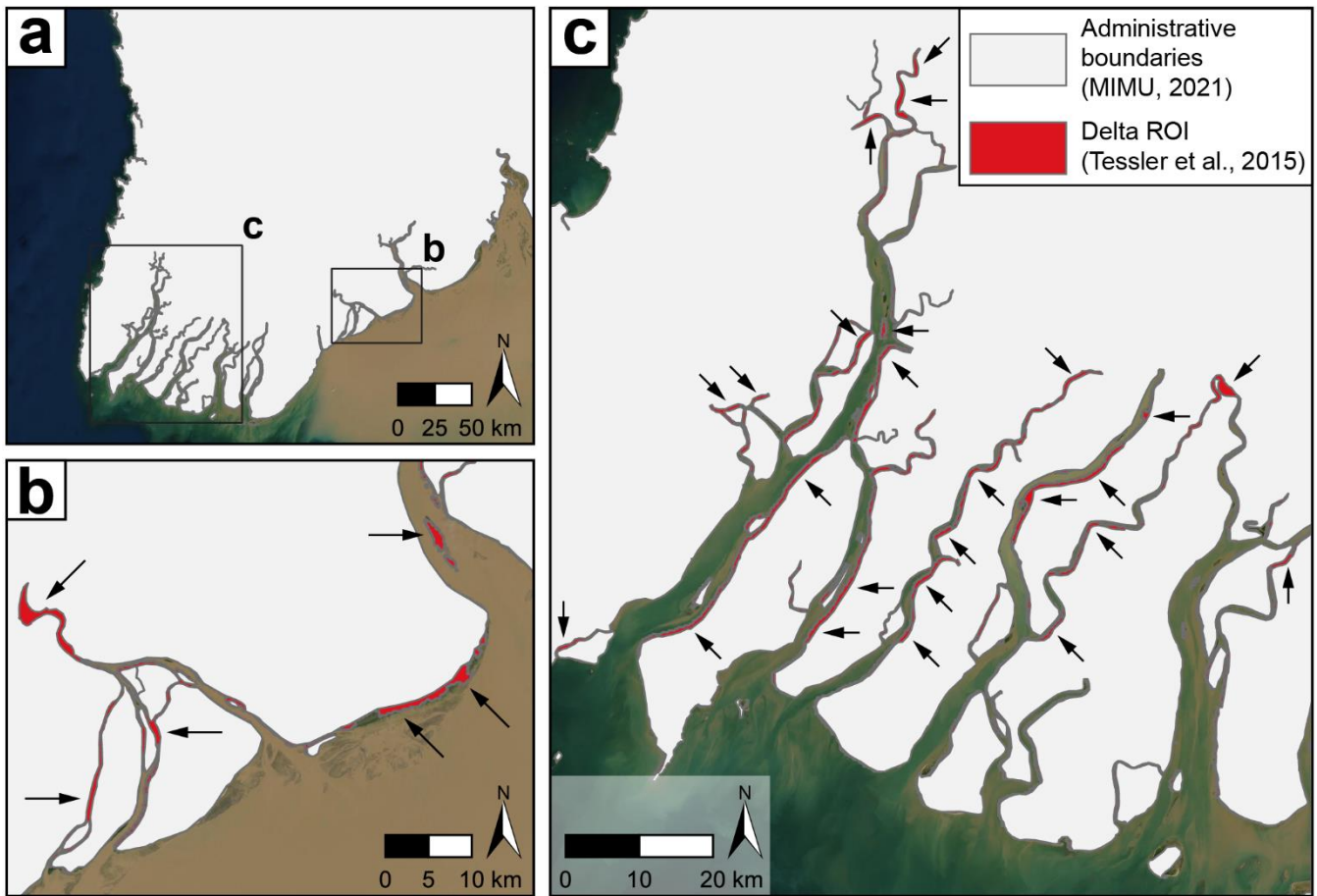


Fig. S28. Discrepancies in delta shape between boundaries of administrative units (MIMU, 2021) and the ROI used in this study (Tessler et al., 2015). Differences along the shore (b) and in river channels (b and c) are indicated by arrows and are ascribed to coastal and fluvial morphodynamics together with different timings of data production. To estimate the impact of SLR on area and population within each administrative district, we used the dataset of MIMU (2021). a), b) and c) are based on Esri World Imagery (2017).

References

Abrams, M., Bailey, B., Tsu, H., and Hato, M.: The ASTER Global DEM, Photogramm. Eng. Remote Sensing, 76:4, 344–348, 2010.

Abrams, M., and Crippen, R.: ASTER GDEM V3 (ASTER Global DEM) User Guide Version 1, Japan's Ministry of Economy, Trade, and Industry (METI), and National Aeronautics and Space Administration (NASA) Jet Propulsion Laboratory/California Institute of Technology, 10 pp., 2019.

Abrams, M., Crippen, R., and Fujisada, H.: ASTER Global Digital Elevation Model (GDEM) and ASTER Global Water Body Dataset (ASTWBD), Remote Sens., 12:7, 1156, <https://doi.org/10.3390/rs12071156>, 2020.

Aguilar, F. J., Aguilar, M. A., Agüera, F., and Sánchez, J.: The accuracy of grid digital elevation models linearly constructed from scattered sample data, Int. J. Geogr. Inf. Sci., 20:2, 169–192, <https://doi.org/10.1080/13658810500399670>, 2006.

Airbus Defence and Space: WorldDEM™ Technical Product Specification Version 2.4, Airbus, 38 pp., 2018.

Airbus Defence and Space: Copernicus Digital Elevation Model Product Handbook Version 3.0, Airbus, 38 pp., 2020.

Altunel, A. O., Okolie, C. J., and Kurtipek, A.: Capturing the level of progress in vertical accuracy achieved by ASTER GDEM since the beginning: Turkish and Nigerian examples, Geocarto Int., <https://doi.org/10.1080/10106049.2022.2063409>, 2022.

Andersen, O. B., Nielsen, K., Knudsen, P., Hughes, C. W., Bingham, R., Fenoglio-Marc, L., Gravelle, M., Kern, M., and Polo, S. P.: Improving the Coastal Mean Dynamic Topography by Geodetic Combination of Tide Gauge and Satellite Altimetry, Mar. Geodesy, 41:6, 517–545, <https://doi.org/10.1080/01490419.2018.1530320>, 2018.

AVISO+: The combined mean dynamic topography MDT CNES-CLS18, <https://www.aviso.altimetry.fr/en/data/products/auxiliary-products/mdt/mdt-description.html>, last access: 7 September 2022.

Berry, P. A. M., Smith, R. G., and Benveniste, J.: ACE2: The New Global Digital Elevation Model, in: Gravity, Geoid and Earth Observation, International Association of Geodesy Symposia 135, edited by Mertiklas, S.P., Springer, Berlin, Heidelberg, Germany, 231–237, https://doi.org/10.1007/978-3-642-10634-7_30, 2010.

Berry, P. A. M., Smith, R., and Benveniste, J.: Altimeter Corrected Elevations, Version 2 (ACE2) [dataset], Palisades, New York: NASA Socioeconomic Data and Applications Center (SEDAC), <https://doi.org/10.7927/H40G3H78>, accessed 2022-03-01, 2019.

Bingham, R. J., Haines, K., and Lea, D. J.: How well can we measure the ocean's mean dynamic topography from space?, *J. Geophys. Res. Oceans*, 119:6, 3336–3356, <https://doi.org/10.1002/2013JC009354>, 2014.

510 Brakenridge, G. R., Syvitski, J. P. M., Niebuhr, E., Overeem, I., Higgins, S. A., Kettner A. J., and Prades, L.: Design with nature: Causation and avoidance of catastrophic flooding, Myanmar, *Earth Sci. Rev.*, 165, 81–109, <https://doi.org/10.1016/j.earscirev.2016.12.009>, 2017.

Brakenridge, G. R., Kettner, A. J., Paris, S., Cohen, S., and Nghiem, S. V.: River and Reservoir Watch Version 4.5, Satellite-based river discharge and reservoir area measurements, 1998–present, DFO Flood Observatory, University of Colorado, USA:

515 <https://floodobservatory.colorado.edu/DischargeAccess.html>, last access: 8 September 2022.

Brill, D., Seeger, K., Pint, A., Reize, F., Kay Thwe Hlaing, Seeliger, M., Opitz, S., Khin Mi Mi Win, Win Thuzar Nyunt, Nilar Aye, Aung Aung, Kyaw Kyaw, Kraas, F., and Brückner, H.: Modern and historical tropical cyclone and tsunami deposits at the coast of Myanmar: Implications for their identification and preservation in the geological record, *Sedimentology*, 67, 1431–1459, <https://doi.org/10.1111/sed.12586>, 2020.

520 Brosens, L., Campforts, B., Govers, G., Aldana-Jague, E., Razanamahandry, V. F., Razafimbelo, T., Rafolisy, T., and Jacobs, L.: Comparative analysis of the Copernicus, TanDEM-X, and UAV-SfM digital elevation models to estimate lavaka (gully) volumes and mobilization rates in the Lake Alaotra region (Madagascar), *Earth Surf. Dynam.*, 10, 209–227, <https://doi.org/10.5194/esurf-10-209-2022>, 2022.

Buckley, S. M., Agram, P. S., Belz, J. E., Crippen, R. E., Gurrola, E. M., Hensley, S., Kobrick, M., Lavalle, M., Martin, J. M.,

525 Neumann, M., Nguyen, Q. D., Rosen, P. A., Shimada, J. G., Simard, M., and Tung, W. W.: NASADEM User Guide, National Aeronautics and Space Administration (NASA) Jet Propulsion Laboratory/California Institute of Technology, Pasadena, California, 48 pp., 2020.

Copernicus Emergency Management Service (© 2015 European Union), [EMSR130] Irrawaddy Delta: Delineation Map, Monitoring 1, 2015.

530 Da Silva, N. A., and Matthews, A. J.: Impact of the Madden–Julian Oscillation on extreme precipitation over the western Maritime Continent and Southeast Asia, *Quarterly Journal of the Royal Meteorological Society*, 147:739, 3434–3453, <https://doi.org/10.1002/qj.4136>, 2021.

de Groot-Reichwein, M. A. M., Goosen, H., and van Steekelenburg, M. G. N.: Climate proofing the Zuidsplassen: a guiding model approach to climate adaptation, *Reg. Environ. Change*, 14, 909–918, <http://dx.doi.org/10.1007/s10113-013-0509-4>,

535 2014.

Department of Meteorology and Hydrology (DMH): General Weather Forecast for 2020 Rainy Season, <https://www.moezala.gov.mm/general-weather-forecast-2020-rainy-season>, last access: 24 August 2022.

Doganalp, S., and Selvi, H. Z.: Local geoid determination in strip area projects by using polynomials, least-squares collocation and radial basis functions, *Measurement* 73, 429–438, <https://doi.org/10.1016/j.measurement.2015.05.030>, 2015.

540 East View Geospatial, Inc.: EVMap50-MMR 1:50,000 Scale Topographic Maps, Minnetonka, Minnesota, 2014.

European Commissions's Directorate-General for European Civil Protection and Humanitarian Aid Operations (ECHO): Vietnam, Laos, Thailand, Myanmar – Tropical Storm NOUL (DG ECHO partners, governments, media), <https://reliefweb.int/report/viet-nam/vietnam-laos-thailand-myanmar-tropical-storm-noul-dg-echo-partners-governments-media>, last access: 24 August 2022, 2020.

545 Farr, T. G., Rosen, P. A., Caro, E., Crippen, R., Duren, R., Hensley, S., Kobrick, M., Paller, M., Rodriguez, E., Roth, L., Seal, D., Shaffer, S., Shimada, J., Umland, J., Werner, M., Oskin, M., Burbank, D., and Alsdorf, D.: The Shuttle Radar Topography Mission, *Rev. Geophys.*, 45:2, RG2004, <https://doi.org/10.1029/2005RG000183>, 2007.

550 Filmer, M. S., Hughes, C. W., Woodworth, P. L., Featherstone, W. E., and Bingham, R. J.: Comparison between geodetic and oceanographic approaches to estimate mean dynamic topography for vertical datum unification: evaluation at Australian tide gauges, *J. Geod.*, 92, 1413–1437, <https://doi.org/10.1007/s00190-018-1131-5>, 2018.

555 Fox-Kemper, B., Hewitt, H. T., Xiao, C., Aðalgeirsdóttir, G., Drijfhout, S. S., Edwards, T. L., Golledge, N. R., Hemer, M., Kopp, R. E., Krinner, G., Mix, A., Notz, D., Nowicki, S., Nurhati, I. S., Ruiz, L., Sallée, J.-B., Slangen, A. B. A., and Yu, Y.: Ocean, Cryosphere and Sea Level Change, in: *Climate Change 2021: The Physical Science Basis. Contribution of Working Group I to the Sixth Assessment Report of the Intergovernmental Panel on Climate Change*, edited by Masson-Delmotte, V., Zhai, P., Pirani, A., Connors, S. L., Péan, C., Berger, S., Caud, N., Chen, Y., Goldfarb, L., Gomis, M. I., Huang, M., Leitzell, K., Lonnoy, E., Matthews, J. B. R., Maycock, T. K., Waterfield, T., Yelekçi, O., Yu, R., and Zhou, B., Cambridge University Press, Cambridge, 9-1–9-257, In press.

560 Garner, G. G., Hermans, T., Kopp, R. E., Slangen, A. B. A., Edwards, T. L., Levermann, A., Nowikci, S., Palmer, M. D., Smith, C., Fox-Kemper, B., Hewitt, H. T., Xiao, C., Aðalgeirsdóttir, G., Drijfhout, S. S., Edwards, T. L., Golledge, N. R., Hemer, M., Kopp, R. E., Krinner, G., Mix, A., Notz, D., Nowicki, S., Nurhati, I. S., Ruiz, L., Sallée, J.-B., Yu, Y., Hua, L., Palmer, T., and Pearson, B.: *IPCC AR6 Sea-Level Rise Projections, Version 20210809*, PO.DAAC, CA, USA, Dataset accessed [2022-05-23] at <https://podaac.jpl.nasa.gov/announcements/2021-08-09-Sea-level-projections-from-the-IPCC-6th-Assessment-Report>, 2021.

Garner, G. G., Kopp, R. E., Hermans, T., Slangen, A. B. A., Koubbe, G., Turilli, M., Jha, S., Edwards, T. L., Levermann, A.,
565 Nowikci, S., Palmer, M. D., and Smith, C.: Framework for Assessing Changes To Sea-level (FACTS), Geoscientific Model
Development, Zenodo [model], <https://zenodo.org/record/6419954>, last access: 22 November 2022, 2022.

German Aerospace Centre (DLR): Earth Observation – Discovering, Surveying, and Understanding Our Planet, DLR, 71 pp.,
2013.

Gesch, D. B.: Best Practices for Elevation-Based Assessments of Sea-Level Rise and Coastal Flooding Exposure, *Front. Earth
570 Sci.*, 6:230, 1–19, <https://doi.org/10.3389/feart.2018.00230>, 2018.

Gorelick, N., Hancher, M., Dixon, M., Ilyushchenko, S., Thau, D., and Moore, R.: Google Earth Engine: Planetary-scale
geospatial analysis for everyone, *Remote Sens. Environ.*, 202, 18–27, <https://doi.org/10.1016/j.rse.2017.06.031>, 2017.

Government of the Union of Myanmar: Myanmar – Post-disaster needs assessment of floods and landslides July–September
2015, Government of the Union of Myanmar, 267 pp., 2015.

575 Guth, P. L., and Geoffroy, T. E.: LiDAR point cloud and ICESat-2 evaluation of 1 second global digital elevation models:
Copernicus wins, *Trans. GIS*, 25:5, 2245–2261, <https://doi.org/10.1111/tgis.12825>, 2021.

Hamden, M. H., Din, A. H. M., Wijaya, D. D., Yusoff, M. Y. M., and Pa’suya, M. F.: Regional Mean Sea Surface and Mean
Dynamic Topography Models Around Malaysian Seas Developed From 27 Years of Along-Track Multi-Mission Satellite
Altimetry Data, *Front. Earth Sci.*, 9, 665876, <https://doi.org/10.3389/feart.2021.665876>, 2021.

580 Hawker, L., Uhe, P., Paulo, L., Sosa, J., Savage, J., Sampson, C., and Neal, J.: A 30 m global map of elevation with forests
and buildings removed, *Environ. Res. Lett.*, 17:2, 024016, <https://doi.org/10.1088/1748-9326/ac4d4f>, 2022.

Hooijer, A., and Vernimmen, R.: Global LiDAR land elevation data reveal greatest sea-level rise vulnerability in the tropics,
Nat. Commun., 12:3592, 1–7, <https://doi.org/10.1038/s41467-021-23810-9>, 2021.

Horton, R., De Mel, M., Peters, D., Lesk, C., Bartlett, R., Helsingin, H., Bader, D., Capizzi, P., Martin, S., and Rosenzweig,
585 C.: Assessing Climate Risk in Myanmar: Technical Report, Center for Climate Systems Research at Columbia University,
WWF-US and WWF-Myanmar, 88 pp., 2017.

Huffman, G. J., Stocker, E. F., Bolvin, D. T., Nelkin, E. J., Tan, J.: GPM IMERG Final Precipitation L3 1 month 0.1 degree x
0.1 degree V06 [dataset], <https://doi.org/10.5067/GPM/IMERGDF/DAY/06>, edited by Savtchenko, A., Greenbelt, Maryland,
Goddard Earth Sciences Data and Information Services Center (GES DISC), last access: 18 June 2021, 2019.

590 Ince, E. S., Barthelmes, F., Reißland, S., Elger, K., Förste, C., Flechtner, F., and Schuh, H.: ICGEM – 15 years of successful collection and distribution of global gravitational models, associated services and future plans, *Earth Sys. Sci. Data*, 11, 647–674, <https://doi.org/10.5194/essd-11-647-2019>, 2019.

Inman, V. L., and Lyons, M. B.: Automated Inundation Mapping Over Large Areas Using Landsat Data and Google Earth Engine, *Remote Sens.*, 12:8, 1348, <https://doi.org/10.3390/rs12081348>, 2020.

595 International Federation of Red Cross and Red Crescent Societies (IFRC): Final Report Myanmar: Floods, IFRC, 31 pp., 2017.

Japan Aerospace Exploration Agency (JAXA): ALOS Global Digital Surface Model “ALOS World 3D – 30m (AW3D30)”, https://www.eorc.jaxa.jp/ALOS/en/dataset/aw3d30/aw3d30_e.htm, last access: 28 October 2022, 2019.

Japan International Cooperation Agency (JICA), Myanmar Survey Department, and Ministry of Forestry: The study on the establishment of geographic database for national rehabilitation and development programme in the Union of Myanmar – 600 Executive Summary, JICA, 86 pp., 2004a.

Japan International Cooperation Agency (JICA), Myanmar Survey Department, and Ministry of Forestry: The study on the establishment of geographic database for national rehabilitation and development programme in the Union of Myanmar – Final Report Volume 1: Main report, JICA, 86 pp., 2004b.

Japan International Cooperation Agency (JICA), Myanmar Survey Department, and Ministry of Forestry: The study on the 605 establishment of geographic database for national rehabilitation and development programme in the Union of Myanmar – Final Report Volume 2: Documents, JICA, 86 pp., 2004c.

Knudsen, P., Bingham, R., Andersen, O., and Rio, M.-H.: A global mean dynamic topography and ocean circulation estimation using a preliminary GOCE gravity model, *J. Geod.*, 85, 861–879, <https://doi.org/10.1007/s00190-011-0485-8>, 2011.

Krieger, G., Moreira, A., Fiedler, H., Hajnsek, I., Werner, M., Younis, M., and Zink, M.: TanDEM-X: A Satellite Formation 610 for High-Resolution SAR Interferometry, *IEEE Trans. Geosci. Remote Sens.*, 45:11, 3317–3341, <https://doi.org/10.1109/TGRS.2007.900693>, 2007.

Kulp, S. A., and Strauss, B. H.: CoastalDEM: A global coastal digital elevation model improved from SRTM using a neural network, *Remote Sens. Environ.*, 206 (1), 231–239, <https://doi.org/10.1016/j.rse.2017.12.026>, 2018.

Kulp, S. A., and Strauss, B. H.: New elevation data triple estimates of global vulnerability to sea-level rise and coastal flooding. 615 *Nat. Commun.*, 10:4844, 1–12, <https://doi.org/10.1038/s41467-019-12808-z>, 2019.

Kulp, S. A., and Strauss, B. H.: CoastalDEM v2.1: A high-accuracy and high-resolution global coastal elevation model trained on ICESat-2 satellite lidar, Climate Central Scientific Report, 17 pp., 2021.

Lemoine, F. G., Smith, D. E., Kunz, L., Smith, R., Pavlis, E. C., Pavlis, N. K., Klosko, S. M., Chinn, D. S., Torrence, M. H., Williamson, R. G., Cox, C. M., Rachlin, K. E., Wang, Y. M., Kenyon, S. C., Salmon, R., Trimmer, R., Rapp, R. H., and Nerem, R. S.: The development of the NASA GSFC and NIMA joint geopotential model, in: Gravity, Geoid and Marine Geodesy, International Association of Geodesy Symposia 117, edited by: Segawa, J., Fujimoto, H., and Okubo, S., Springer, Berlin, Heidelberg, https://doi.org/10.1007/978-3-662-03482-8_62, 1997.

Marešová, J., Gdulová, K., Pracná, P., Moravec, D., Gábor, L., Prošek, J., Barták, V., and Moudrý, V.: Applicability of Data Acquisition Characteristics to the Identification of Local Artefacts in Global Digital Elevation Models: Comparison of the Copernicus and TanDEM-X DEMs, *Remote Sens.*, 13:19, 3931, <https://doi.org/10.3390/rs13193931>, 2021.

Masson-Delmotte, V., Zhai, P., Pirani, A., Connors, S. L., Péan, C., Berger, S., Caud, N., Chen, Y., Goldfarb, L., Gomis, M. I., Huang, M., Leitzell, K., Lonnoy, E., Matthews, J. B. R., Maycock, T. K., Waterfield, T., Yelekçi, O., Yu, R., and Zhou, B. (Eds.): Climate Change 2021: The Physical Science Basis. Contribution of Working Group I to the Sixth Assessment Report of the Intergovernmental Panel on Climate Change, Cambridge University Press, 2021.

Mayer-Gürr, T., Kvas, A., Klinger, B., Rieser, D., Zehentner, N., Pail, R., Gruber, T., Fecher, T., Rexer, M., Schuh, W.-D., Kusche, J., Brockmann, J., Loth, I., Müller, S., Eicker, A., Schall, J., Baur, O., Höck, E., Krauss, S., and Maier, A.: The new combined satellite only model GOCO05s, EGU General Assembly 2015, Vienna, Austria, 12–17 April 2015, EGU2015-12364, <http://dx.doi.org/10.13140/RG.2.1.4688.6807>, 2015.

Mehmood, H., Conway, C., and Perera, D.: Mapping of Flood Areas Using Landsat with Google Earth Engine Cloud Platform, *Atmosphere*, 12:7, 866, <https://doi.org/10.3390/atmos12070866>, 2021.

Mi Mi Tun: Country Report of Myanmar, Department of Disaster Management, Ministry of Social welfare, Relief and Resettlement, 8 pp., 2020.

Minderhoud, P. S. J., Coumou, L., Erkens, G., Middelkoop, H., and Stouthamer, E.: Mekong delta much lower than previously assumed in sea-level rise impact assessments, *Nat. Commun.*, 10:3847, 1–13, <https://doi.org/10.1038/s41467-019-11602-1>, 2019.

Myanmar Information Management Unit (MIMU): Seasonal Flooding as of 26th July 2017, MIMU, MIMU1515v01, 2017.

Myanmar Information Management Unit (MIMU): Probable Flood Inundated Ayeyarwady and Bago (West) Region (as of 1st September 2020), MIMU, MIMU1515v01, 2020.

Myanmar Information Management Unit (MIMU): MIMU Geospatial Data,

645 <http://geonode.themimu.info/layers/?limit=100&offset=0>, last access: 28 October 2022, 2021.

Ministry of Economy, Trade and Industry (METI) of Japan, National Aeronautics and Space Administration (NASA), and United States Geological Survey: ASTER Global DEM Validation Summary Report, 28 pp., 2009.

Moharrami, M., Javanbakht, M., and Attarchi, S.: Automatic flood detection using sentinel-1 images on the google earth engine, *Environ. Monit. Assess.*, 193, 248, <https://doi.org/10.1007/s10661-021-09037-7>, 2021.

650 Mukul, M., Srivastava, V., Jade, S., and Mukul, M.: Uncertainties in the Shuttle Radar Topography Mission (SRTM) Heights: Insights from the Indian Himalaya and Peninsula, *Sci. Rep.*, 7, 41672, <https://doi.org/10.1038/srep41672>, 2017.

Mulet, S., Rio, M.-H., Etienne, H., Artana, C., Cancet, M., Dibarboure, G., Hui Feng, Husson, R., Picot, N., Provost, C., and Strub, P. T.: The new CNES-CLS18 global mean dynamic topography, *Ocean Sci.*, 17, 789–808, <https://doi.org/10.5194/os-17-789-2021>, 2021.

655 National Aeronautics and Space Administration (NASA): Giovanni – The Bridge Between Data and Science v 4.37, <https://giovanni.gsfc.nasa.gov/giovanni/>, last access: 18 June 2021.

National Aeronautics and Space Administration (NASA) Jet Propulsion Laboratory (JPL): NASA Shuttle Radar Topography Mission Water Body Data Shapefiles & Raster Files, <https://doi.org/10.5067/MEaSUREs/SRTM/SRTMSWBD.003>, last access: 8 February 2022, 2013.

660 National Aeronautics and Space Administration (NASA) Jet Propulsion Laboratory (JPL), Shuttle Radar Topography Mission, <https://www2.jpl.nasa.gov/srtm/mission.htm>, last access: 26 August 2022, 2016.

Neuenschwander, A. L., Pitts, K. L., Jelley, B. P., Robbins, J., Klotz, B., Popescu, S. C., Nelson, R. F., Harding, D., Pederson, D., and Sheridan, R.: ATLAS/ICESat-2 L3A Land and Vegetation Height, Version 4, NASA National Snow and Ice Data Center, Boulder, Colorado, USA, 18 pp., <https://doi.org/10.5067/ATLAS/ATL08.004>, 2021.

665 Peter, B. G., Cohen, S., Lucey, R., Munasinghe, D., Raney, A., and Brakenridge, G. R.: Google Earth Engine Implementation of the Floodwater Depth Estimation Tool (FwDET-GEE) for Rapid and Large Scale Flood Analysis, *IEEE Geosci. Remote. Sens. Lett.*, 19, 1–5, <https://doi.org/10.1109/LGRS.2020.3031190>, 2020.

Rabus, B., Eineder, M., Roth, A., and Bamler, R.: The shuttle radar topography mission – a new class of digital elevation models acquired by spaceborne radar, *ISPRS J. Photogramm. Remote Sens.*, 57:4, 241–262, [https://doi.org/10.1016/S0924-6702\(02\)00124-7](https://doi.org/10.1016/S0924-6702(02)00124-7), 2003.

Rio, M.-H., Mulet, S., and Picot, N.: Beyond GOCE for the ocean circulation estimate: Synergetic use of altimetry, gravimetry, and in situ data provides new insight into geostrophic and Ekman currents, *Geophys. Res. Lett.*, 41:24, 8918–8925, 2014.

Rizzoli, P., Martone, M., Gonzalez, C., Wecklich, C., Tridon, D. B., Bräutigam, B., Bachmann, M., Schulze, D., Fritz, T., Huber, M., Wessel, B., Krieger, G., Zink, M., and Moreira, A.: Generation and performance assessment of the global TanDEM-X elevation model, *ISPRS J. Photogramm. Remote Sens.*, 132, 119–139, <https://doi.org/10.1016/j.isprsjprs.2017.08.008>, 2017.

Rodríguez, E., Morris, C. S., Belz, J. E., Chapin, E. C., Martin, J. M., Daffer, W., and Hensley, S.: An Assessment of the SRTM Topographic Products, National Aeronautics and Space Administration (NASA) Jet Propulsion Laboratory (JPL), Technical Report JPL D-31639, 143 pp., 2005.

Rose, A., McKee, J., Sims, K., Bright, E., Reith, A., and Urban, M.: LandSScan Global 2020 [dataset], Oak Ridge National Laboratory, <https://doi.org/10.48690/1523378>, 2021.

Siart, C., Bubenzer, O., and Eitel, B.: Combining digital elevation data (SRTM/ASTER), high resolution satellite imagery (Quickbird) and GIS for geomorphological mapping: A multi-component case study on Mediterranean karst in Central Crete, *Geomorphology*, 112:1–2, 106–121, <https://doi.org/10.1016/j.geomorph.2009.05.010>, 2009.

Smith, R. G., and Berry, P. A. M.: ACE2: Global Digital Elevation Model User Guide, 22 pp., 2009.

685 Specialised Information Service Cartography and Geodata (SIS Maps): Topo List, <https://kartographie.staatsbibliothek-berlin.de/en/about-us/map-catalogs/topo-list/>, last access: 29 March 2021.

Tachikawa, T., Kaku, M., Iwasaki, A., Gesch, D., Oimoen, M., Zhang, Z., Danielson, J., Krieger, T., Curtis, B., Haase, J., Abrams, M., Crippen, R., and Carabajal, C.: ASTER Global Elevation Model Version 2 – Summary of Validation Results, National Aeronautics and Space Administration (NASA) Land Processes Distributed Active Archive Center, and Joint Japan-US ASTER Science Team, 26 pp., 2011.

Tadono, T., Nagai, H., Ishida, H., Oda, F., Naito, S., Minakawa, K., and Iwamoto, H.: Generation of the 30 m-mesh global digital surface model by ALOS Prism, in: *Int. Arch. Photogramm. Remote Sens. Spatial Inf. Sci.*, XLI-B4, XXIII ISPRS Congress, Prague, Czech Republic, 12–19 July 2016, 157–162, <https://doi.org/10.5194/isprs-archives-XLI-B4-157-2016>, 2016.

695 Takaku, J., Tadono, T., and Tsutsui, K.: Generation of high resolution global DSM from ALOS Prism, in Int. Arch. Photogramm. Remote Sens. Spatial Inf. Sci., XL-4, ISPRS Technical Commission IV Symposium, Suzhou, China, 14–16 May 2014, 243–248, <https://doi.org/10.5194/isprsarchives-XL-4-243-2014>, 2014.

Talchabhadel, R., Nakagawa, H., Kawaike, K., Yamanoi, K., and Thapa, B. R.: Assessment of vertical accuracy of open source 30m resolution space-borne digital elevation models, Geomatics, Nat. Hazards Risk, 12:1, 939–960, 700 <https://doi.org/10.1080/19475705.2021.1910575>, 2021.

Tessler, Z. D., Vörösmarty, C. J., Grossberg, M., Gladkova, I., Aizenman, H., Syvitski, J. P. M., and Foufoula-Georgiou, E.: Profiling risk and sustainability in coastal deltas of the world, Science 349:6248, 638–643, <https://doi.org/10.1126/science.aab3574>, 2015.

Tripathy, P., and Malladi, T.: Global Flood Mapper: a novel Google Earth Engine application for rapid flood mapping using 705 Sentinel-1 SAR, Nat. Hazards, 114, 1341–1363, <https://doi.org/10.1007/s11069-022-05428-2>, 2022.

United Nations Platform for Space-based Information for Disaster Management and Emergency Response (UN-SPIDER): SAR-Flood mapping using a change detection approach, https://www.un-spider.org/sites/default/files/Code_GEE_flood_mapping.txt, last access: 22 June 2021, 2019.

UN Office for the Coordination of Humanitarian Affairs (OCHA): Myanmar: Humanitarian Update on Monsoon Season 710 Floods, 21 July 2017, OCHA, Situation Report, <https://reliefweb.int/report/myanmar/myanmar-humanitarian-update-monsoon-season-floods-21-july-2017>, 2017.

UN Office for the Coordination of Humanitarian Affairs (OCHA): Myanmar: Floods and Landslides – Jun 2018, <https://reliefweb.int/disaster/fl-2018-000124-mmr>, last access: 24 August 2022, 2018.

UN Office for the Coordination of Humanitarian Affairs (OCHA): Myanmar: Floods and Landslides – Jun 2020, 715 <https://reliefweb.int/disaster/fl-2020-000172-mmr>, last access. 24 August 2022, 2020.

Vernimmen, R., Hooijer, A., and Pronk, M.: New ICESat-2 Satellite LiDAR Data Allow First Global Lowland DTM Suitable for Accurate Coastal Flood Risk Assessment, Remote Sens., 12:17, 2827, <https://doi.org/10.3390/rs12172827>, 2020.

Wechsler, S. P.: Uncertainties associated with digital elevation models for hydrologic applications: a review, Hydrol. Earth Syst. Sci., 11, 1481–1500, <https://doi.org/10.5194/hess-11-1481-2007>, 2007.

720 Wendleder, A., Wessel, B., Roth, A., Breunig, M., Martin, K., and Wagenbrenner, S.: TanDEM-X Water Indication Mask: Generation and First Evaluation Results, *IEEE J. Sel. Top. Appl. Earth Obs. Remote Sens.*, 6:1, 171–179, <https://doi.org/10.1109/JSTARS.2012.2210999>, 2012.

Wessel, B.: TanDEM-X Ground Segment – DEM Products Specification Document, EOC, DLR, Oberpfaffenhofen, Germany, Public Document TD-GS-PS-0021, Issue 3.2, [Online], Available: <https://tandemx-science.dlr.de/>, 2018.

725 Wessel, B., Huber, M., Wohlfahrt, C., Marschalk, U., Kosmann, D., and Roth, A.: Accuracy assessment of the global TanDEM-X Digital Elevation Model with GPS data, *ISPRS J. Photogramm. Remote Sens.*, 139, 171–182, <https://doi.org/10.1016/j.isprsjprs.2018.02.017>, 2018.

Li, X.: Using radial basis functions in airborne gravimetry for local geoid improvement, *J. Geod.*, 92, 471–485, <https://doi.org/10.1007/s00190-017-1074-2>, 2018.

730 Yamaguchi, Y., Kahle, A. B., Tsu, H., Kawakami, T., and Pniel, M.: Overview of Advanced Spaceborne Thermal Emission and Reflection Radiometer (ASTER), *IEEE Trans. Geosci. Remote Sens.*, 36:4, 1062–1071, <https://doi.org/10.1109/36.700991>, 1998.

Zin Mie Mie Sein, Zhi, X., Ullah, I., Azam, K., Ngoma, H., Saleem, F., Yun Xing, Iyakaremye, V., Syed, S., Hina, S., and Nkunzimana, A.: recent variability of sub-seasonal monsoon precipitation and its potential drivers in Myanmar using in-situ 735 observation during 1981–2020, *Int. J. Climatol.*, 42:6, 3341–3359, <https://doi.org/10.1002/joc.7419>, 2022.